



This is a repository copy of *A decentralised neural model explaining optimal integration of navigational strategies in insects*.

White Rose Research Online URL for this paper:

<https://eprints.whiterose.ac.uk/162675/>

Version: Published Version

Article:

Sun, X., Yue, S. and Mangan, M. orcid.org/0000-0002-0293-8874 (2020) A decentralised neural model explaining optimal integration of navigational strategies in insects. *eLife*, 9. ISSN 2050-084X

<https://doi.org/10.7554/elife.54026>

Reuse

This article is distributed under the terms of the Creative Commons Attribution (CC BY) licence. This licence allows you to distribute, remix, tweak, and build upon the work, even commercially, as long as you credit the authors for the original work. More information and the full terms of the licence here:

<https://creativecommons.org/licenses/>

Takedown

If you consider content in White Rose Research Online to be in breach of UK law, please notify us by emailing eprints@whiterose.ac.uk including the URL of the record and the reason for the withdrawal request.



eprints@whiterose.ac.uk
<https://eprints.whiterose.ac.uk/>

1 A Decentralised Neural Model

2 Explaining Optimal Integration of

3 Navigational Strategies in Insects

4 Xuelong Sun¹, Shigang Yue^{1,3†}, Michael Mangan^{2†}

*For correspondence:

syue@lincoln.ac.uk;
m.mangan@sheffield.ac.uk;
xsun@lincoln.ac.uk

†Joint last authorship

5 ¹Computational Intelligence Lab & L-CAS, School of Computer Science, University of
6 Lincoln, United Kingdom; ²Sheffield Robotics, Department of Computer Science,
7 University of Sheffield, Sheffield, United Kingdom; ³Machine Life and Intelligence
8 Research Centre, Guangzhou University, China

9

10 **Abstract** Insect navigation arises from the coordinated action of concurrent guidance systems
11 but the neural mechanisms through which each functions, and are then coordinated, remains
12 unknown. We propose that insects require distinct strategies to retrace familiar routes
13 (route-following) and directly return from novel to familiar terrain (homing) using different aspects
14 of frequency encoded views that are processed in different neural pathways. We also demonstrate
15 how the Central Complex and Mushroom Bodies regions of the insect brain may work in tandem to
16 coordinate the directional output of different guidance cues through a contextually switched
17 ring-attractor inspired by neural recordings. The resultant unified model of insect navigation
18 reproduces behavioural data from a series of cue conflict experiments in realistic animal
19 environments and offers testable hypotheses of where and how insects process visual cues, utilise
20 the different information that they provide and coordinate their outputs to achieve the adaptive
21 behaviours observed in the wild.

23 Introduction

24 Central-place foraging insects navigate using a 'toolkit' of independent guidance systems (*Wehner,*
25 *2009*) of which the most fundamental are path integration (PI), whereby foragers track the distance
26 and direction to their nest by integrating the series of directions and distances travelled (for reviews
27 see *Heinze et al. (2018); Collett (2019)*), and visual memory (VM), whereby foragers derive a homing
28 signal by comparing the difference between current and stored views (for reviews see *Zeil (2012);*
29 *Collett et al. (2013)*). Neurophysiological and computational modelling studies advocate the central
30 complex neuropil (CX) as the PI centre (*Heinze and Homberg, 2007; Seelig and Jayaraman, 2015;*
31 *Stone et al., 2017*), whereas the mushroom body neuropils (MB) appear well suited to assessing
32 visual valence as needed for VM (*Heisenberg, 2003; Ardin et al., 2016; Müller et al., 2018*). Yet,
33 two key gaps in our understanding remain. Firstly, although current VM models based on the
34 MB architecture can replicate route following (RF) behaviours whereby insects visually recognise
35 the direction previously travelled at the same position (*Ardin et al., 2016; Müller et al., 2018*), they
36 cannot account for visual homing (VH) behaviours whereby insects return directly to their familiar
37 surroundings from novel locations following a displacement (e.g. after being blown off course by
38 a gust of wind) (*Wystrach et al., 2012*). Secondly, despite increasing neuroanatomical evidence
39 suggesting that premotor regions of the CX coordinate navigation behaviour (*Pfeiffer and Homberg,*
40 *2014; Heinze and Pfeiffer, 2018; Honkanen et al., 2019*), a theoretical hypothesis explaining how

41 this is achieved by the neural circuitry has yet to be developed. In this work we present a unified
 42 neural navigation model that extends the core guidance modules from two (PI and VM) to three (PI,
 43 RF, and VH) and by integrating their outputs optimally using a biologically realistic ring attractor
 44 network in the CX produces realistic homing behaviours.

45 The foremost challenge in realising this goal is to ensure that the core guidance subsystems
 46 provide sufficient directional information across conditions. Contemporary VM models based on
 47 the MBs can replicate realistic RF behaviours in complex visual environments (ant environments:
 48 *Kodzhabashev and Mangan (2015); Ardin et al. (2016)*, bee environments: *Müller et al. (2018)*)
 49 but do not generalise to visual homing scenarios whereby the animal must return directly to
 50 familiar terrain from novel locations (ants: *Narendra (2007)*, bees: *Cartwright and Collett (1982)*,
 51 wasps: *Stürzl et al. (2016)*). Storing multiple nest-facing views before foraging, inspired by observed
 52 learning walks in ants (*Müller and Wehner, 2010; Fleischmann et al., 2016*) and flights in bees and
 53 wasps (*Zeil et al., 1996; Zeil and Fleischmann, 2019*), provides a potential solution (*Graham et al.,*
 54 *2010; Wystrach et al., 2013*), but simulation studies have found this approach to be brittle due to
 55 high probabilities of aligning with the wrong memory causing catastrophic errors (*Dewar et al.,*
 56 *2014*). Moreover, ants released perpendicularly to their familiar route do not generally align with
 57 their familiar visual direction as predicted by the above algorithms (*Wystrach et al., 2012*), but
 58 instead move directly back towards the route (*Fukushi and Wehner, 2004; Kohler and Wehner,*
 59 *2005; Narendra, 2007; Mangan and Webb, 2012; Wystrach et al., 2012*), which would require a
 60 multi-stage mental alignment of views for current models. New computational hypothesis are thus
 61 required that can guide insects directly back to their route (often moving perpendicularly to the
 62 habitual path), but also allow for the route direction to be recovered (now aligned with the habitual
 63 path) upon arrival at familiar surroundings (see *Figure 1A "Zero Vector"*).

64 With the necessary elemental guidance systems defined, a unifying model must then convert
 65 the various directional recommendations into a single motor command appropriate to the context
 66 (*Cruse and Wehner, 2011; Hoinville et al., 2012; Collett et al., 2013; Webb, 2019*). Behavioural stud-
 67 ies show that when in unfamiliar visual surroundings ("Off-Route") insects combine the outputs of
 68 their PI and VH systems (*Collett, 1996; Bregy et al., 2008; Collett, 2012*) relative to their respective
 69 certainties consistent with optimal integration theory (*Legge et al., 2014; Wystrach et al., 2015*)
 70 (*Figure 1A "Full Vector"*). Upon encountering their familiar route, insects readily recognise their
 71 surroundings, recover their previous bearing and retrace their familiar path home (*Harrison et al.,*
 72 *1989; Kohler and Wehner, 2005; Wystrach et al., 2011; Mangan and Webb, 2012*). Thus, the naviga-
 73 tion coordination model must possess two capabilities: (a) output a directional signal consistent
 74 with the optimal integration of PI and VH when Off-Route (b) switch from Off-Route (PI and VH) to
 75 On-Route (RF) strategies when familiar terrain is encountered. Mathematical models have been
 76 developed that reproduce aspects of cue integration in specific scenarios (*Cruse and Wehner, 2011;*
 77 *Hoinville and Wehner, 2018*), but to date no neurobiologically constrained network revealing how
 78 insects might realise these capabilities has been developed.

79 To address these questions a functional modelling approach is followed that extends the current
 80 base model described by *Webb (2019)* to (a) account for the ability of ants to home from novel
 81 locations back to the familiar route before retracing their familiar path the rest of the journey home,
 82 and (b) propose a neurally-based model of the central complex neuropil that integrates compet-
 83 ing cues optimally and generates a simple steering command that can drive behaviour directly.
 84 Performance is bench-marked by direct comparison to behavioural data reported by *Wystrach*
 85 *et al. (2012)* (showing different navigation behaviours on and off the route), *Legge et al. (2014);*
 86 *Wystrach et al. (2015)* (demonstrating optimal integration of PI and VM), and through qualitative
 87 comparison to extended homing paths where insects switch between strategies according to the
 88 context (*Narendra, 2007*). Biological realism is enforced by constraining models to the known
 89 anatomy of specific brain areas, but where no data exists an exploratory approach is taken to
 90 investigate the mechanisms that insects may exploit. *Figure 1A* depicts the adaptive behaviours
 91 observed in animals that we wish to replicate accompanied by a functional overview of our unified

92 model of insect navigation (*Figure 1B*) mapped to specific neural sites (*Figure 1C*).

93 Results

94 Mushroom bodies as drivers of rotational invariant visual homing

95 For ants to return directly to their familiar route after a sideways displacement (*Figure 1A* "Zero Vec-
96 tor") without continuous mental or physical realignment they require access to rotational invariant
97 visual cues. *Stone et al. (2018)* recently demonstrated that binary images of panoramic skylines
98 converted into their frequency components can provide such a rotationally-invariant encoding of
99 scenes in a compact form (see *Image processing* for an introduction to frequency transformations
100 of images). Moreover, they demonstrated that the difference between the rotationally invariant
101 features (the **amplitudes** of the frequency coefficients) between two locations increases monotonically
102 with distance producing an error surface reminiscent of the image difference surfaces reported
103 by *Zeil et al. (2003)* which can guide an agent back to familiar terrain. Here we investigate whether
104 the MB neuropils shown capable of assessing the visual valence of learned rotationally-varying
105 panoramic skylines for RF (*Ardin et al., 2016; Müller et al., 2018*), might instead assess the visual
106 valence of rotationally-invariant properties of views sampled along a familiar route supporting
107 visual homing.

108 To this end, the intensity sensitive input neurons of *Ardin et al. (2016)*'s MB model are replaced
109 with input neurons encoding rotational invariant **amplitudes** (*Figure 2A* left, blue panel). The
110 network is trained along an 11*m* curved route in a simulated world that mimics the training regime
111 of ants in *Wystrach et al. (2012)* (see *Methods and Materials* and *Reproduce visual navigation*
112 *behaviour* for details on simulated world, image processing, model architecture and training and
113 test regime). After training, the firing rate of the MB output neuron (MBON) when placed at locations
114 across the environment at random orientations reveals a gradient that increases monotonically
115 with distance from the familiar route area, providing a homing signal sufficient for VH independent
116 of the animal's orientation (*Figure 2C*).

117 Motor output is then generated by connecting the MBON to a steering network recently located
118 in the fan-shaped body (FB/CBU) of the CX that functions by minimising the difference between
119 the animal's current and desired headings (*Stone et al., 2017*). *Stone et al. (2017)*'s key insight
120 was that the anatomically observed shifts of activity in the columnar neurons that encode the
121 desired heading in essence simulate 45° turns left and right, and thus by comparing the summed
122 differences between the activity profiles of these predicted headings to the current heading then
123 the appropriate turning command can be computed (see *Figure 2B*). We adopt this circuit as the
124 basis for computing steering commands for all strategies as suggested by *Honkanen et al. (2019)*.

125 In the proposed VH model the current heading input to the steering circuit uses the same
126 celestial global compass used in *Stone et al. (2017)*'s PI model. Insects track their orientation
127 through head-direction cells (*Seelig and Jayaraman, 2015*) whose concurrent firing pattern forms
128 a single bump of activity that shifts around the ring as the animal turns (measured through local
129 visual (*Green et al., 2017; Turner-Evans et al., 2017*), global visual (*Heinze and Homberg, 2007*)
130 and proprioceptive (*Seelig and Jayaraman, 2015*) cues). Neuroanatomical data (*Kim et al., 2017;*
131 *Turner-Evans et al., 2019; Pisokas et al., 2019*) supports theoretical predictions (*Cope et al., 2017;*
132 *Kakaria and de Bivort, 2017*) that the head-direction system of insects follows a ring attractor (RA)
133 connectivity pattern characterised by local excitatory interconnections between direction selective
134 neurons and global inhibition. In this work, the global compass RA network is not modelled directly
135 but rather we simulate its sinusoidal activity profile in a ring of I-TB1 (locusts and $\Delta 7$ of flies) neurons
136 found in the protocerebral bridge (PCB/PB) (*Figure 2A* green ring) (see *Current headings*).

137 A desired heading is then generated by copying the current activity pattern of the global compass
138 neurons to a new neural ring which we speculate could reside in either a distinct subset of I-TB1
139 neurons (*Beetz et al., 2015*) or in the FB. Crucially, the copied activity profile also undergoes a
140 leftward shift proportional to any increase in visual novelty (a similar shifting mechanisms has been

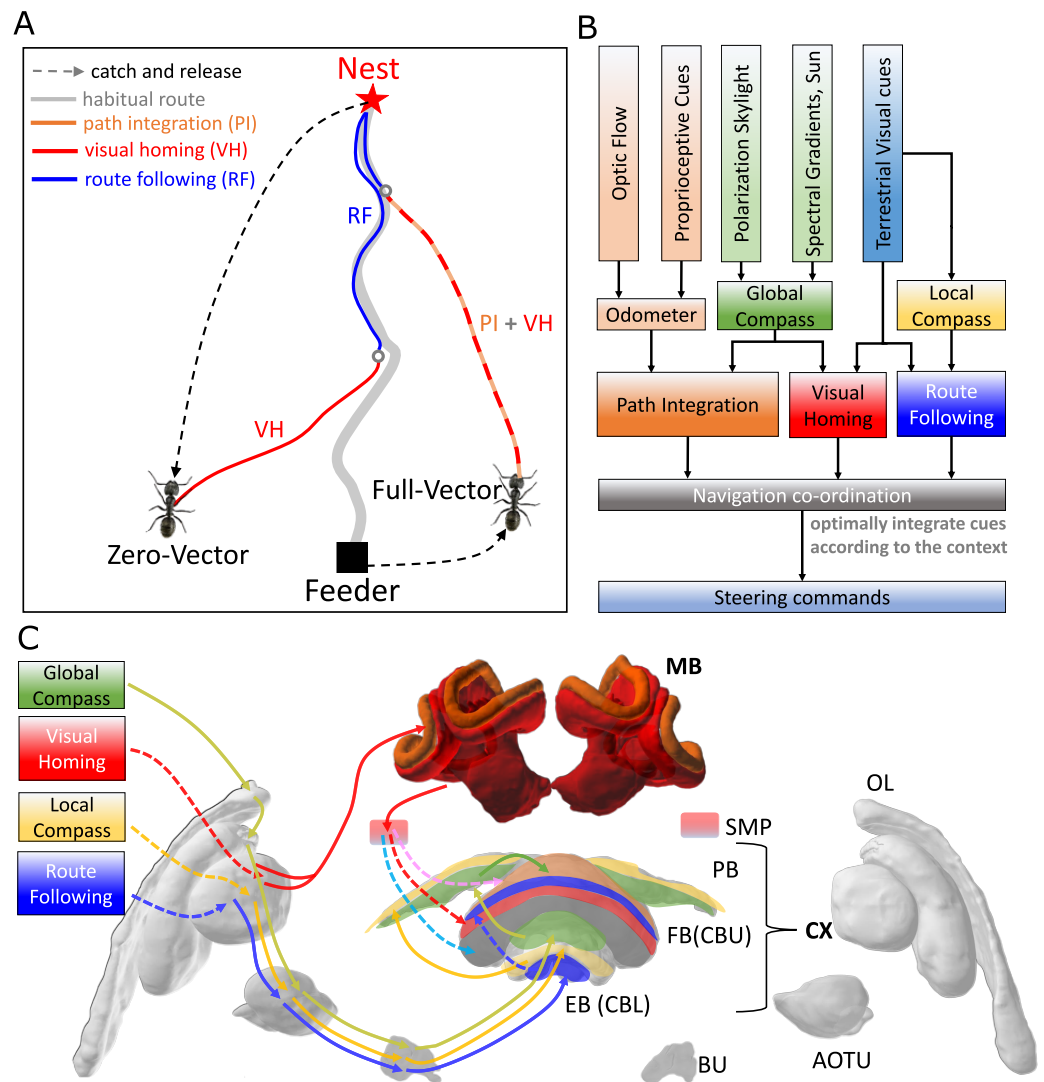
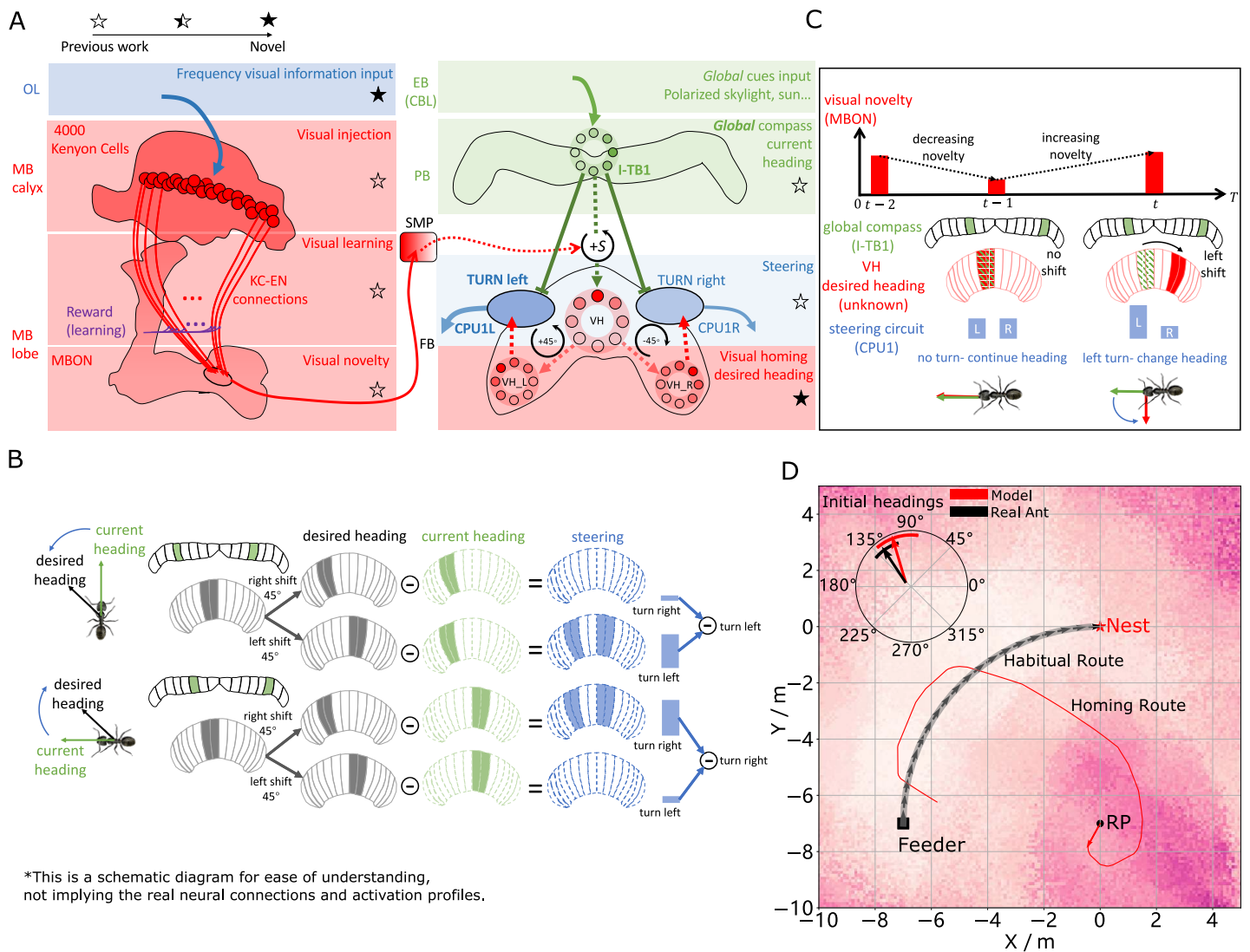


Figure 1. Overview of the unified navigation model and its homing capabilities. (A) The homing behaviours to be produced by the model when displaced either from the nest and having no remaining PI home vector (zero vector), or from the nest with a full home vector (full vector). Distinct elemental behaviours are distinguished by coloured path segments, and stripped bands indicate periods where behavioural data suggests that multiple strategies are combined. Note that this colour coding of behaviour is maintained throughout the remaining figures to help the reader map function to brain region. (B) The proposed conceptual model of the insect navigation toolkit from sensory input to motor output. Three elemental guidance systems are modelled in this paper: path integration (PI), visual homing (VH) and route following (RF). Their outputs must then be coordinated in an optimal manner appropriate to the context before finally outputting steering command. (C) The unified navigation model maps the elemental guidance systems to distinct processing pathways: **RF**: OL -> AOTU -> BU -> CX; **VH**: OL -> MB -> SMP -> CX; **PI**: OL -> AOTU -> BU -> CX. The outputs are then optimally integrated in the proposed ring attractor networks of the FB in CX to generate a single motor steering command. Connections are shown only for the left brain hemisphere for ease of visualisation but in practice are mirrored on both hemispheres. Hypothesised or assumed pathways are indicated by dashed lines whereas neuroanatomically supported pathways are shown by solid lines (a convention maintained throughout all figures).

OL: optic lobe, AOTU: anterior optic tubercle, CX: central complex, PB: protocerebrum bridge, FB: fan-shape body (or CBU: central body upper), EB: ellipsoid body (or CBL: central body lower), MB: mushroom body, SMP: superior medial protocerebrum, BU: bulb.

Images of the brain regions are adapted from the insect brain database <https://www.insectbraindb.org>.



*This is a schematic diagram for ease of understanding, not implying the real neural connections and activation profiles.

Figure 2. Visual Homing in the Insect Brain. (A) Neural model of visual homing. Rotational-invariant **amplitudes** are input to the MB calyx which are then projected to the Kenyon cells (KCs) before convergence onto the MB output neuron (MBON) which seeks to memorise the presented data via reinforcement learning based plasticity (for more details see *Visual homing*) (MB circuit: left panels). SMP neurons measure positive increases in visual novelty (through input from the MBON) which causes a shift between the current heading (green cells) and desired headings (red cells) in the rings of the CX (SMP pathway between MB and CX: centre panel; CX circuit: right panels). The CX-based steering circuit then computes the relevant turning angle. Example activity profiles are shown for an increase in visual novelty, causing a shift in desired heading and a command to change direction. Each model component in all figures is labelled with a shaded star to indicate what aspects are new versus those incorporated from previous models (see legend in upper left). (B) Schematic of the steering circuit function. First the summed differences between the impact of 45° left and right turns on the desired heading and the current heading are computed. By comparing the difference between the resultant activity profiles allows an appropriate steering command to be generated. (C) Schematic of the visual homing model. When visual novelty drops ($t - 2$ to $t - 1$) the desired heading is an unshifted copy of the current heading so the current path is maintained but when the visual novelty increases ($t - 1$ to t) the desired heading is shifted from the current heading. (D) The firing rate of the MBON sampled across locations at random orientations is depicted by the heat-map showing a clear gradient leading back to the route. The grey curve shows the habitual route along which ants were trained. RP (release point) indicates the position where real ants in *Wystrach et al. (2012)* were released after capture at the nest (thus zero-vector) and from which simulations were started. The ability of the VH model to generate realistic homing data is shown by the initial paths of simulated ants which closely match those of real ants (see inserted polar plot showing the mean direction and 95% confidential interval), and also the extended example path shown (red line). Note that once the agent arrives in the vicinity of the route, it appears to meander due the flattening of visual novelty gradient and the lack of directional information.

Figure 2-source data 1. The frequency information for the locations with random orientations across the world.

Figure 2-source data 2. The visual homing results of the model

141 proposed for the head-direction system (*Green et al., 2017; Turner-Evans et al., 2017*) which we
 142 propose is measured by neurons in the superior medial protocerebrum (SMP) (*Aso et al., 2014;*
 143 *Plath et al., 2017*) (see *Figure 2A* centre and activity of red rings). The result is a mechanism
 144 that recommends changing direction when the agent moves away from familiar terrain (visual
 145 novelty increases) but recommends little change to the current heading when the visual novelty is
 146 decreasing (see *Figure 2C* for a schematic of the VH mechanism). We note that there is a distinction
 147 between a ring network which describes a group of neurons whose pattern of activity forms a
 148 circular representation regardless of actual physical arrangement and RA networks which follow
 149 a specific connectivity pattern (all modelled RAs labelled in figures). Taken together the model
 150 iteratively refines its orientation to descend the visual novelty gradient and thus recover familiar
 151 terrain (see *Figure 2A* for full model).

152 *Figure 2D* demonstrates that the proposed network accurately replicates both the directed
 153 initial paths as in *Wystrach et al. (2012)* (see the inserted black arrow), and extended homing paths
 154 as in *Narendra (2007)* observed in ants displaced to novel locations perpendicular to their familiar
 155 routes. We note that upon encountering the route the model is unable to distinguish the direction
 156 in which to travel and thus meanders back and forth along the familiarity valley, unlike real ants,
 157 demonstrating the need for additional route recognition and recovery capabilities.

158 **Optimally integrating visual homing and path integration**

159 We have demonstrated how ants could use visual cues to return to the route in the absence of
 160 PI but in most natural scenarios (e.g. displacement by a gust of wind) ants will retain a home
 161 vector readout offering an alternative, and often conflicting, guidance cue to that provided by VH.
 162 In such scenarios desert ants strike a compromise by integrating their PI and VH outputs in a manner
 163 consistent with optimal integration theory by weighting VH relative to the familiarity of the current
 164 view (*Legge et al., 2014*) and PI relative to the home vector length (a proxy for directional certainty)
 165 (*Wystrach et al., 2015*).

166 Various ring-like structures of the CX represent directional cues as bumps of activity with the
 167 peak defining the specific target direction, and the spread providing a mechanism to encode cue
 168 certainty as required for optimal integration (for an example see increased spread of HD cell activity
 169 when only proprioceptive cues are present (*Seelig and Jayaraman, 2015*)). Besides their excellent
 170 properties to encode the animal's heading ring attractors also provide a biologically realistic means
 171 to optimally weight cues represented in this format (*Touretzky, 2005; Sun et al., 2018*) without the
 172 need for dedicated memory circuits to store means and uncertainties of each cue.

173 Thus we introduce a pair of integrating ring-attractor networks to the CX model (*Figure 3A* grey
 174 neural rings: RA_L and RA_R) that take as input the desired headings from the above proposed
 175 VH model (red neural rings: VH_L and VH_R) and *Stone et al. (2017)*'s PI model (orange neural
 176 rings: PI_L and PI_R) and output combined Off Route desired heading signals that are sent to the
 177 steering circuits (blue neural rings: CPU_L and CPU_R). *Stone et al. (2017)* mapped the home vector
 178 computation to a population of neurons (CPU4) owing to their dual inputs from direction selective
 179 compass neurons (I_TB1) and motion sensitive speed neurons (TN2) as well as their recurrent
 180 connectivity patterns facilitating accumulation of activity as the animal moves in a given direction.
 181 *Wystrach et al. (2015)* showed that the certainty of PI automatically scales with the home-vector
 182 length owing to the accumulating effect of the memory neurons which correlates with directional
 183 uncertainty, and thus the output PI network is directly input to the ring attractor circuits. In our
 184 implementation the VH input has a fixed height and width profile and influences the integration
 185 through tuning neurons (TUN) (see the plotted activation function in *Figure 3B* and *Optimal cue*
 186 *integration*) that we suggest reside in the SMP and modulate the PI input to the integration network.
 187 Altering the weighting in this manner rather than by scaling the VH input independently allows VH
 188 to dominate the integrated output at sites with high visual familiarity even in the presence of a
 189 large home vector without having large stored activity. We note however, that both approaches
 190 remain feasible and further neuroanatomical data is required to clarify which, if either, mechanism

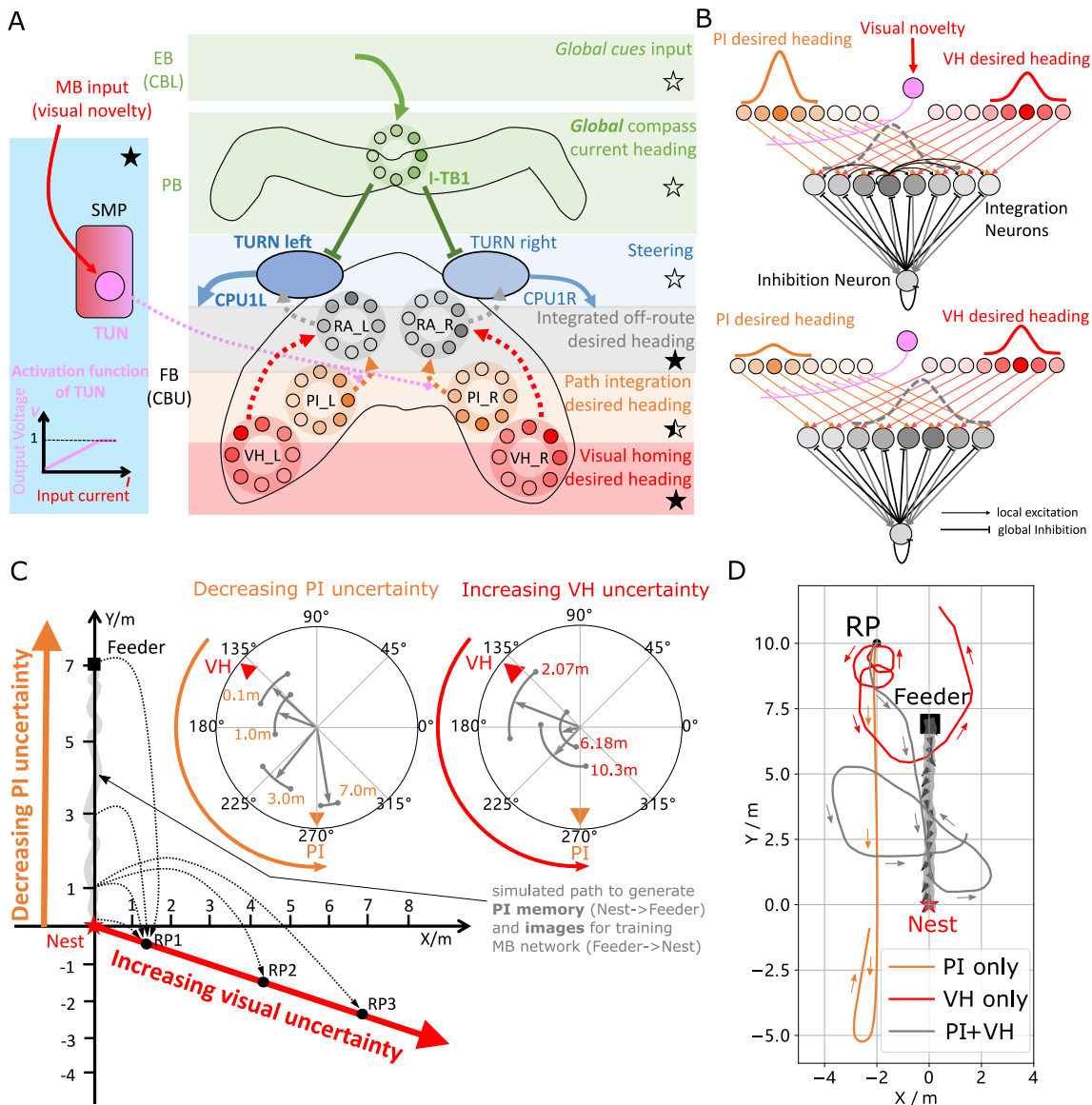


Figure 3. Optimal cue integration in the CX. (A) Proposed model for optimally integrating PI and VH guidance systems. In each hemisphere, ring attractors (RAs) (grey neural rings) (speculatively located in FB/CBU) receive the corresponding inputs from PI (orange neural rings) and VH (red neural rings) with the outputs sent to the corresponding steering circuits (blue neural rings). Integration is weighted by the visual novelty tracking neuron (TUN) whose activation function is shown in the leftmost panel. (B) Examples of optimal integration of PI and VH headings for two PI states with the peak stable state (grey dotted activity profile in the integration neurons) shifting towards VH as the home vector length recedes. (C) Replication of optimal integration studies of *Wystrach et al. (2015)* and *Legge et al. (2014)*. Simulated ants are captured at various points (0.1m, 1m, 3m and 7m) along their familiar route (grey curve) and released at release point 1 (RP1) thus with the same visual certainty but with different PI certainties as in *Wystrach et al. (2015)* (see thick orange arrow). The left polar plot shows the initial headings of simulated ants increasingly weight their PI system (270°) in favour of their VH system (135°) as the home vector length increases and PI directional uncertainty drops. Simulated ants are also transferred from a single point 1m along their familiar route to ever distant release points (RP1, RP2, RP3) thus with the same PI certainty but increasingly visual uncertainty as in *Legge et al. (2014)* (see thick red arrow). The right polar plot shows the initial headings of simulated ants increasingly weight PI (270°) over VH (135°) as visual certainty drops. (see *Reproduce the optimal cue integration behaviour for details*) (D) Example homing paths of the independent and combined guidance systems displaced from the familiar route (grey) to a fictive release point (RP)

Figure 3–Figure supplement 1. The extended homing paths and the PI memory in the simulations

Figure 3–source data 1. The results of tuning PI uncertainty.

Figure 3–source data 2. The results of tuning VH uncertainty.

Figure 3–source data 3. The extended homing path of PI, VH and combined PI and VH.

192 **Figure 3C** shows the initial headings produced by the model which replicates the trends reported
 193 in cue-conflict experiments by *Legge et al. (2014)* and *Wystrach et al. (2015)* when the uncertainty
 194 of PI and VH cues were altered independently. Example extended paths of independent PI and
 195 VH models and the ring-attractor-based combined PI and VH model are plotted in **Figure 3D** with
 196 the combined model showing the most ant-like behaviour (*Kohler and Wehner, 2005; Mangan and*
 197 *Webb, 2012*) by initially following predominantly the home-vector direction before switching to
 198 visual homing when the home-vector length drops leading the simulated ant back to familiar terrain.
 199 Note that the PI-only and PI+VH models are drawn back towards their fictive nest sites indicated
 200 by their home vectors which if left to run would likely result in emergent search-like patterns as
 201 in *Stone et al. (2017)*. Moreover, upon encountering the route the VH-based models (VH-only and
 202 PI+VH) are unable to distinguish the direction in which to travel and hence again (see meander
 203 around the valley of familiarity **Figure 2D** and **Figure 3D**) further demonstrating a need for a route
 204 recovery mechanism.

205 **Route following in the insect brain**

206 The model described above can guide insects back to their familiar route area, but lacks the means
 207 to recover the route direction upon arrival as observed in homing insects. This is not surprisingly
 208 as VH relies upon translationally-varying but rotational-invariant information whereas RF requires
 209 rotationally-varying cues. Thus we introduce a new elemental guidance system that makes use of
 210 the rotationally-varying *phase* coefficients of the frequency information derived from the panoramic
 211 skyline which tracks the orientation of specific features of the visual surroundings (see *Methods*
 212 *and Materials*). Here we ask whether by associating the rotationally invariant **amplitudes** (shown
 213 useful for place recognition) with the rotationally-varying *phases* experienced at those locations,
 214 insects might recover the familiar route direction.

215 Neuroanatomical data with which to constrain a model remains sparse and therefore a standard
 216 artificial neural network (ANN) architecture is used to investigate the utility of *phase*-based route
 217 recovery with biological plausibility discussed in more detail below. A 3-layer ANN was trained to
 218 associate the same 81 rotational-invariant **amplitudes** as used in the VH model with the rotational
 219 varying *phase* value of single frequency coefficient experienced when travelling along the habitual
 220 route which we encode in an 8 neuron-ring (see **Figure 4A** and *Route Following* for detailed model
 221 description). Thus, when the route is revisited the network should output the orientation that the
 222 *phase* converged upon when at the same location previously, which we note is not necessarily
 223 aligned with the actual heading of the animal (e.g. it may track the orientation to vertical bar (*Seelig*
 224 *and Jayaraman, 2015*)). Realignment is possible using the same steering mechanism as described
 225 above but which seeks to reduce the offset between the current *phase* readout (e.g. a local compass
 226 locked onto visual features of the animals surroundings), and the recalled *phase* readout from the
 227 ANN.

228 We speculate that the most likely neural pathways for the new desired and current headings are
 229 from Optic Lobe via Anterior Optic Tubercle (AOTU) and Bulb (BU) to EB (CBL) of the CX (*Homberg*
 230 *et al., 2003; Omoto et al., 2017*) (see **Figure 4A**) with the desired heading terminating in the EB
 231 whereas the current heading continues to the PB forming a local compass that sits beside the global
 232 compass used by PI and VH systems. This hypothesis is further supported by the recently identified
 233 parallel pathways from OL via AOTU to the CX in *Drosophila* (*Timaeus et al., 2020*). That's to say that,
 234 firstly, there are two parallel pathways forming two compass systems- the global (here based on
 235 celestial cues) and the local (based on terrestrial cues) compasses modelled by the activation of I-TB1
 236 and II-TB1 neurons respectively. Four classes of CL1 neurons (or E-PG and P-EG neurons) *Heinze*
 237 *and Homberg (2009); Xu et al. (2020)* and three classes of independent TB1 neurons *Betz et al.*
 238 *(2015)* have been identified that provide potential sites for the parallel recurrent loops encoding
 239 independent local and global compasses. Secondly, the desired heading, which is the recalled
 240 *phase* of a specific view, is generated through the neural plasticity from AOTU to BU and BU to EB,
 241 which is line with recent evidence of associative learning between the R-neurons transmitting visual

242 information from BU to EB and the compass neurons (CL1a or E-PG neurons) that receive input
 243 from EB (Kim *et al.*, 2019; Fisher *et al.*, 2019). This kind of learning endows the animal with the
 244 ability to flexibly adapt their local compass and also desired navigational orientation according to
 245 the changing visual surroundings. Hanesch *et al.* (1989) reported a direct pathway from EB to FB
 246 neurons which we model to allow comparison of the local compass activity (II-TB1) with the desired
 247 heading. However, we note that this connectivity has not been replicated in recent studies Heinze
 248 and Homberg (2008) and thus further investigation of potential pathways is required.

249 The RF model accurately recovers the initial route heading in a similar manner to real ants
 250 returned to the start of their familiar route (Wystrach *et al.*, 2012) (Figure 4B, insert), and then
 251 follows the remaining route in its entirety back to the nest again reflecting ant data (Kohler and
 252 Wehner, 2005; Mangan and Webb, 2012) (Figure 4B). The quiver plots displayed in the background
 253 of Figure 4B show the preferred homing direction output by the ANN when rotated on the spot
 254 across locations in the environment. The noise in the results are due to errors in the tracking
 255 performance (see examples Figure 4B right) yet as these errors are in largely confined to the
 256 magnitude, the steering circuit still drives the ant along the route. We note that this effect is
 257 primarily a function of the specific frequency transformation algorithm used which we borrow
 258 from computer graphics to investigate the utility of frequency encoding of visual information. The
 259 biological realism of such transforms and their potential implementation in the insect vision system
 260 are addressed in the Discussion. The displaced routes also highlight the danger of employing
 261 solely RF which often shadows rather than converges with the route when displaced sideways,
 262 further demonstrating the necessity for integration with the Off-Route strategies that promote
 263 route convergence.

264 **Route recovery through context-dependent modulation of guidance systems**

265 Homing insects readily recognise familiar route surroundings, recover their bearing, and retrace
 266 their habitual path home, irrespective of the status of other guidance system such as PI. Replicating
 267 such context-dependent behavioural switching under realistic conditions is the final task for the
 268 proposed model. The visual novelty measured by the MBON provides an ideal signal for context
 269 switching with low output when close to the route when RF should dominate versus high output
 270 further away from the route when PI and VH should be engaged (see Figure 2D). Also the fact that
 271 Off-route strategies (PI and VH) compute their turning angles with reference to the global compass
 272 whereas the On-route RF strategy is driven with reference to a local compass provides a means to
 273 modulate their inputs to the steering circuit independently. This is realised through a non-linear
 274 weighting of the On and Off-route strategies which we propose acts through the same SMP pathway
 275 as the VH model (see the SN1 and SN2 neurons in Figure 5A) (see Context-dependent switch for
 276 neuron details and Figure 7 for a force-directed graph representation of the final unified model).

277 The activity of the proposed switching circuit and the paths that it generates in simulated zero
 278 vector and full vector displacement trials are shown in Figure 5 B & C respectively. In the full vector
 279 trial (Figure 5B (upper), Figure 5C (solid line)) as visual novelty is initially high (see high TUN activity
 280 until step 78) SN2 is activated which enables Off-Route strategies (PI and VH) while SN1 (always the
 281 inverse of SN2) is deactivated which disables On-Route strategies. Note that it is the integration of PI
 282 and VH that generates the direct path back to the route area in the FV trial: PI recommends moving
 283 at a 45° bearing but VH prevents ascension of the visual novelty gradient that this would cause with
 284 the compromise being a bearing closer to 90° i.e. toward the route. As the route is approached
 285 the visual novelty decreases (again see TUN activity), until at step 78 SN2 falls below threshold
 286 and deactivates the Off-Route strategies while conversely SN1 activates and engages On-Route
 287 strategies. After some initial flip-flopping while the agents converges on the route (steps 78-85) RF
 288 becomes dominant and drives the agent back to the nest via the familiar path. In the zero vector
 289 trial (Figure 5B (lower), Figure 5B (dashed line)) Off-route strategies (here only VH) largely dominate
 290 (some false positive route recognition (e.g step 60)) until the route is recovered (step 93), at which
 291 point the same flip-flopping during route convergence occurs (steps 93-96) followed by RF alone

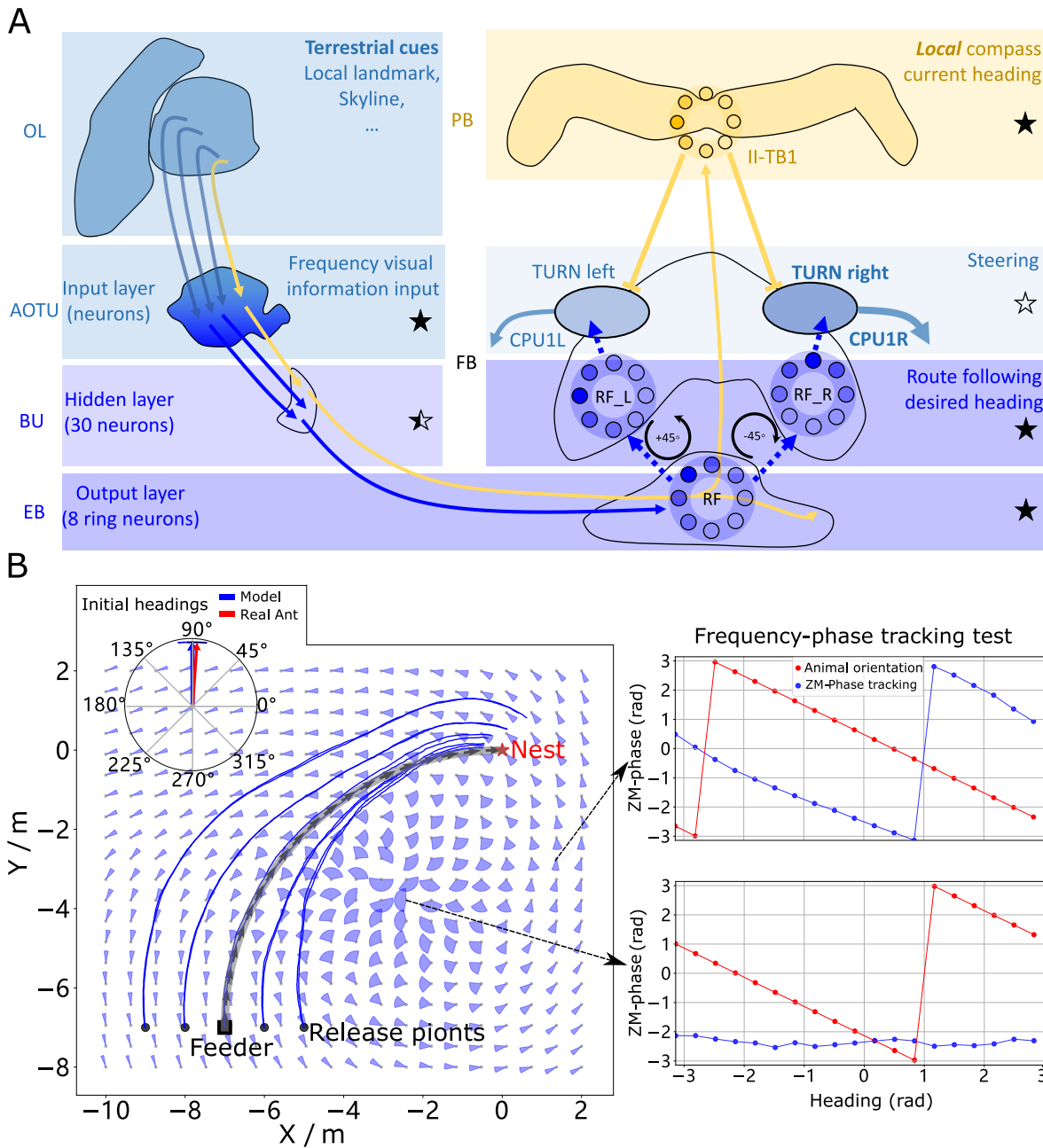


Figure 4. Phase-based route following. (A) Neural model. The visual pathway from the optic lobe via AOTU and Bulb to EB of the CX is modelled by a fully connected artificial neural network (ANN) with one hidden layer. The input layer receives the **amplitudes** of the frequency encoded views (as for the MB network) and the output layer is an 8-neuron ring whose population encoding represents the desired heading against to which the agent should align. (B) Behaviours. Blue and red arrows in the inserted polar plot (top left) display the mean directions and 95% confidential intervals of the initial headings of real (*Wystrach et al., 2012*) and simulated ants released at the start of the route (-7, -7) respectively. Dark blue curves show the routes followed by the model when released at 5 locations close to the start of the learned path. The overlaid fan-plots indicate the circular statistics (the mean direction and 95% confidential interval) of the homing directions recommended by the model when sampled across heading directions (20 samples at 18° intervals). Data for entire rotations are shown on the right for specific locations with the upper plot, sampled at (1.5, -3), demonstrating accurate phase-based tracking of orientation, whereas the lower plot sampled at (-2.5, -3.5) shows poor tracking performance and hence produces a wide fan-plot.

Figure 4-source data 1. The frequency tracking performance across the world.

Figure 4-source data 2. The RF model results of the agents released on route.

Figure 4-source data 3. The RF model results of the agents released aside from the route.

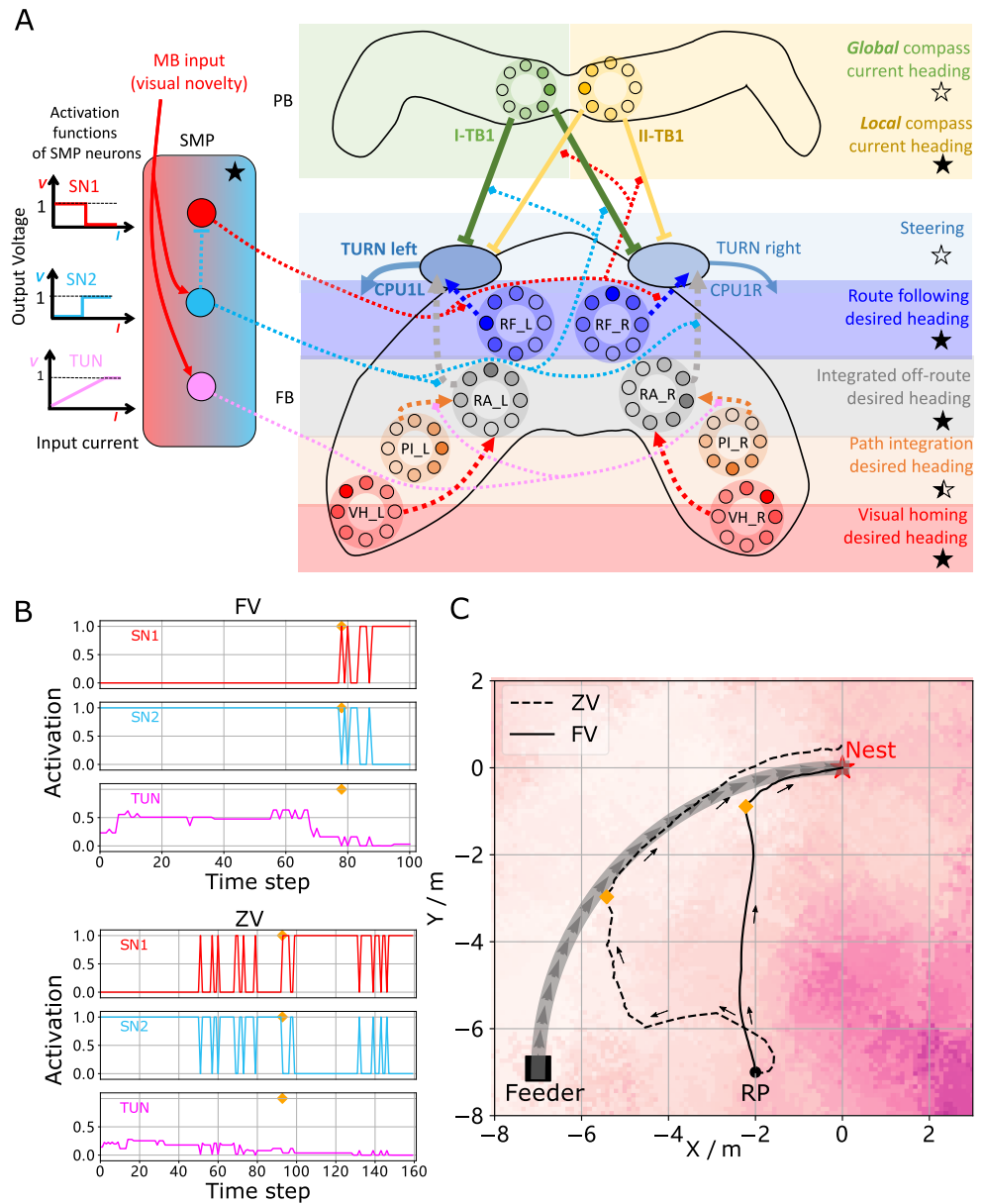


Figure 5. Unified model realising the full array of coordinated navigational behaviours. (A)

Context-dependent switching is realised using two switching neurons (SN1, SN2) that have mutually exclusive firing states (one active while the other is inactive) allowing coordination between On and Off-Route strategies driven by the instantaneous visual novelty output by the MB. Connectivity and activation functions of the SMP neurons are shown in the left side of panel. **(B)** Activation history of the SN1, SN2 and TUN (to demonstrate the instantaneous visual novelty readout of the MB) neurons during the simulated displacement trials. **(C)** Paths generated by the unified model under control of the context-dependent switch circuit during simulated FV (solid line) and ZV (dashed line) displacement trials.

Figure 5-source data 1. The navigation results of the whole model.

292 which returns the agent to the nest via the familiar path. It should be noted that the data presented
 293 utilised different activation functions of the TUN neuron that weights PI and VH (see **Table 2** for
 294 parameter settings across trials and **Discussion** for insights into model limitations and potential
 295 extensions), yet the results presented nevertheless provide a proof-of-principle demonstration that
 296 the proposed unified navigation model can fulfil all of the criteria defined for replication of key
 297 adaptive behaviour observed in insects (**Figure 1A**).

298 Discussion

299 This work addresses two gaps in the current understanding of insect navigation: what are the core
300 visual guidance systems required by the insect navigational toolkit? And how are they coordinated
301 by the insect brain?

302 We propose that the insect navigation toolkit (*Wehner, 2009; Webb, 2019*) should be extended to
303 include independent visual homing (VH) and route following (RF) systems (see *Figure 1B* for updated
304 Insect Navigation Toolkit). We show how VH and RF can be realised using frequency-encoding of
305 panoramic skylines to separate information into rotationally-invariant **amplitudes** for VH and
306 rotationally-varying *phases* for RF. The current model utilises frequency encoding schema from the
307 computer graphics but behavioural studies support the use of spatial frequency by bees (*Horridge,*
308 *1997; Lehrer, 1999*), with neurons in the lobula of dragonflies (*O'Carroll, 1993*) and locusts (*James*
309 *and Osorio, 1996*) found to have receptive fields akin to basis functions, providing a mechanism by
310 which to extract the frequency information necessary for the local compass system. Our model
311 allows for this information extraction process to happen at multiple stages ahead of its usage in
312 the central learning sites such as the MBs opening the possibility for its application in either the
313 optic lobes or subsequent pathways through regions such as the AOTU. Further, neurophysiological
314 data is required to pinpoint both the mechanisms and sites of this data processing in insects.
315 Similarly, following *Stone et al. (2017)* the global compass signal directly mimics the firing pattern
316 of compass neurons in the CX without reference to sensory input but *Gkanias et al. (2019)* recently
317 presented a plausible neural model of the celestial compass processing pipeline that could be
318 easily integrated into the current model to fill this gap. Follow-on neuroanatomically constrained
319 modelling of the optic lobes presents the most obvious extension of this work allowing the neural
320 pathway from sensory input to motor output signal to be mapped in detail. Conversely, modelling
321 the conversion of direction signals into behaviour via motor generating mechanisms such as central
322 pattern generators (see (*Steinbeck et al., 2020*)) will then allow closure of the sensory-motor loop.

323 Visual homing is modelled on neural circuits found along the OL-MB-SMP pathway (*Ehmer and*
324 *Gronenberg, 2002; Gronenberg and López-Riquelme, 2004*) before terminating in the CX steering
325 circuit (*Stone et al., 2017*) and shown capable of producing realistic homing paths. In this schema
326 the MBs do not measure rotationally-varying sensory valence as recently used to replicate RF (*Ardin*
327 *et al., 2016; Müller et al., 2018*), but rather the spatially varying (but rotationally-invariant) sensory
328 valence more suited to gradient descent strategies such as visual homing (*Zeil et al., 2003; Stone*
329 *et al., 2018*) and other taxis behaviours (*Wystrach et al., 2016*). This is inline with the hypothesis
330 forwarded by *Collett and Collett (2018)* that suggest that the MBs output "whether" the current
331 sensory stimulus is positive or negative and the CX then adapts the animal heading, the "whither",
332 accordingly.

333 Route following is shown possible by learned associations between the **amplitudes** (i.e. the
334 place) and the *phase* (the orientation) experienced along a route, allowing realignment when later at
335 a proximal location. This kind of neural plasticity based correlation between the visual surroundings
336 and the orientations fits with data recently observed in fruit flies (*Kim et al., 2019; Fisher et al.,*
337 *2019*). These studies provide the neural explanation for the animal's ability to make flexible use of
338 visual information to navigate while the proposed model gives a detailed implementation of such
339 ability in the context of insect's route following schema. Neurophysiological evidence suggests that
340 the layered visual pathway from OL via AOTU and BU to the EB of the CX (*Barth and Heisenberg,*
341 *1997; Homberg et al., 2003; Omoto et al., 2017*) with its suggested neural plasticity properties (*Barth*
342 *and Heisenberg, 1997; Yilmaz et al., 2019*) provides a possible neural pathway but further analysis
343 is needed to identify the circuit structures that might underpin the generation of RF desired heading.
344 In addition to the desired heading, the current heading of RF is derived from the local compass
345 system anchored to animal's immediate visual surroundings. This independent compass system
346 may be realised parallel to the global compass system in an similar but independent circuit (*Heinze*
347 *and Homberg, 2009; Beetz et al., 2015; Xu et al., 2020*). Our model therefore hypothesises that

348 insects possess different compass systems based on varied sensory information and further that
 349 insects possess the capability (via CX-based RAs) to coordinate their influence optimally according
 350 to the current context. Since the global compass, the local compass and the desired heading of RF
 351 share the same visual pathway (OL->AOTU->BU->CX), distinct input and output patterns along this
 352 pathway may be found by future neuroanatomical studies. In addition, in the proposed model, the
 353 activation of current heading and desired heading of RF overlap in the EB, and therefore separation
 354 of activation profiles representing each output (e.g. following methods in *Seelig and Jayaraman*
 355 (2015)) presents another meaningful topic for future neurophysiological research.

356 Closed-loop behavioural studies during which the spatial frequency information of views is
 357 altered (similar to *Paulk et al. (2015)*) coincident with imaging of key brain areas (*Seelig and Jayara-*
 358 *man, 2013, 2015*) offers a means to investigate which neural structures make use of what visual
 359 information. Complimentary behavioural experiments could verify the distinct VH and RF systems
 360 by selectively blocking the proposed neural pathways with impacts on behaviour predicted by
 361 *Figure 2C* and *Figure 4B* respectively. *Ofstad et al. (2011)* report that visual homing abilities are lost
 362 for fruit flies with a blocked EB of the CX but not MB, which is predicted by our model if animals have
 363 learned target-facing views to which they can later align using their RF guidance system. Analysis of
 364 animal's orientation during learning is thus vital to unpacking precisely how the above results arise.

365 With the elemental guidance strategies defined, we propose that their outputs are coordinated
 366 through the combined action of the MBs and CX. Specifically, we demonstrate that a pair of
 367 ring attractor networks that have similar connectivity patterns of the CX-based head-direction
 368 system (*Kim et al., 2017; Turner-Evans et al., 2019; Pisokas et al., 2019*), are sufficient for optimally
 369 weighting multiple directional cues from the same frame of reference (e.g. VH and PI). The use of a
 370 pair of integrating RAs is inspired by the column structure of the FB which has 16 neural columns
 371 divided into two groups of 8 neural columns that each represent the entire 360° space. The optimal
 372 integration of PI and VH using a ring attractor closely matches the networks theorised to govern
 373 optimal directional integration in mammals (*Jeffery et al., 2016*) and supports hypothesis of their
 374 conserved use across animals (*Sun et al., 2018*). Optimality is secured either through adapting the
 375 shape of the activity profile of the input as is the case for PI which naturally scales with distance,
 376 or by using a standardised input activity profile with cross-inhibition of competing cues as is the
 377 case for VH in the model. The later schema avoids the need for ever increasing neural activity to
 378 maintain relevance.

379 To replicate the suite of navigational behaviours described in *Figure 1* our network includes
 380 three independent ring attractor networks: the global compass head direction system (*Pisokas*
 381 *et al., 2019*); the local compass head direction system (*Seelig and Jayaraman, 2015; Kim et al.,*
 382 *2017; Turner-Evans et al., 2019*); and an Off-route integration system (modelled here). We would
 383 speculate that it is likely that central place foraging insects also possess a similar integration network
 384 for "On-Route" cues (not modelled here) bringing the total number of RAs to four. The utility of
 385 RAs for head-direction tracking arises from their properties in converging activity to a signal bump
 386 that can easily be shifted by sensory input and is maintained in the absence of stimulation. In
 387 addition, RAs also possess the beneficial property that they spontaneously weight competing
 388 sensory information stored as bumps of activity in an optimal manner. Thus, there are excellent
 389 computational reasons for insects to invest in such neural structures. Yet, it should be clear that the
 390 model proposed here represents a proof-of-concept demonstrating that the underlying network
 391 architectures already mapped to the CX (directional cues encoded as bumps of activity (*Seelig and*
 392 *Jayaraman, 2015; Heinze and Homberg, 2007*); various lateral shifting mechanisms (*Stone et al.,*
 393 *2017; Green et al., 2017; Turner-Evans et al., 2017*); RAs (*Kim et al., 2017; Turner-Evans et al., 2019;*
 394 *Pisokas et al., 2019*)) are sufficient to generate adaptive navigation but further studies are required
 395 to critique and refine the biological realism of this hypothesis.

396 While this assemblage recreates optimal integration of strategies that share a compass system,
 397 it does not easily extend to integration of directional cues from other frames of reference (e.g. VH
 398 and PI reference the global compass versus RF that references a local compass). Indeed as the

399 CX steering network seeks to minimise the difference between a current and a desired heading,
 400 calibrating input signals from different frames of reference would require a similar calibration of
 401 their respective compass systems. Rather, the proposed model incorporates a context-dependent
 402 non-linear switching mechanism driven by the output of the MB that alternates between strategies:
 403 global compass based PI and VH are triggered when the surroundings are unfamiliar, but when
 404 in familiar surroundings engage local compass based RF. In summary, the adaptive behaviour
 405 demonstrated is the result of distinct guidance systems that converge in the CX, with their relative
 406 weighting defined by the output of the MB. This distributed architecture is reminiscent of mecha-
 407 nisms found in the visual learning of honeybees (*Plath et al., 2017*), and supports the hypothesis
 408 that the CX is the navigation coordinator of insects (*Heinze, 2017; Honkanen et al., 2019*) but shows
 409 how the MB acts as a mediator allowing the CX to generate optimal behaviour according to the
 410 context.

411 The resultant unified model of insect navigation *Figure 1B* and *C* represents a proof-of-principle
 412 framework as to how insects might co-ordinate core navigational behaviours (PI, VH and RF) under
 413 standard field manipulations *Figure 1A*. Neuroanatomical data has been drawn from across insect
 414 classes (see *Table 1*) to ensure neural realism where possible with performance compared to ant
 415 navigation behaviour in a single simulated desert ant habitat. The framework can be easily extended
 416 to new navigation behaviours observed in other insects from idiothetic PI (*Kim and Dickinson, 2017*)
 417 to straight line following (*El Jundi et al., 2016*) to migrations (*Reppert et al., 2016*) as well as more
 418 nuanced strategies that flexibly use directional cues from different sensory modalities (*Wystrach*
 419 *et al., 2013; Schwarz et al., 2017; Dacke et al., 2019*). A priority of future works should be the
 420 investigation of the differences and commonalities in sensory systems, neural structures and
 421 ecology of different insect navigators and how they impact behaviour allowing for extension and
 422 refinement of the framework for different animals. Complementary stress-testing of models across
 423 different environments in both simulation and robotic studies are also required to ensure that
 424 model performance generalises across species and habitats and to provide guidance to researchers
 425 seeking the sensory, processing and learning circuits underpinning these abilities.

426 **Methods and Materials**

427 All source code related to this publication is available for download at [https://github.com/XuelongSun/](https://github.com/XuelongSun/InsectNavigationToolkitModelling)
 428 [InsectNavigationToolkitModelling](https://github.com/XuelongSun/InsectNavigationToolkitModelling). All simulations and network models are implemented by Python
 429 3.5 and make use of external libraries-*numpy, matplotlib, scipy, PIL* and *cv2*.

430 **Simulated 3D world**

431 The environment used in this study is that provided by *Stone et al. (2018)* which is itself adapted
 432 from *Baddeley et al. (2012)* (see *Figure 6C*). It is a virtual ant-like world consisting of randomly
 433 generated bushes, trees and tussocks based on triangular patches (for more details see *Baddeley*
 434 *et al. (2012)*). Therefore, the data of this simulated world is stored in a matrix with the size of
 435 $N_p \times 3 \times 3$, defining the three dimensional coordinates (x,y,z) of the three vertices of N_p (number of
 436 patches) triangle patches. Agent movement was constrained to a $20m \times 20m$ training and test area
 437 allowing free movement without the requirement of an additional obstacle avoidance mechanism.

438 **Image reconstruction**

439 The agent's visual input at location (x, y) with the heading direction θ_h is simulated from a point
 440 1 cm above from the ground plane with field of view 360° wide by 90° high (centred on the horizon).
 441 This panoramic image (300×104) is then wrapped onto a sky-centred disk as required by the
 442 Zernike Moments transformation algorithm used with the size of $208(104 \times 2) \times 208$ ready for image
 443 processing (see *Figure 6D* upper).

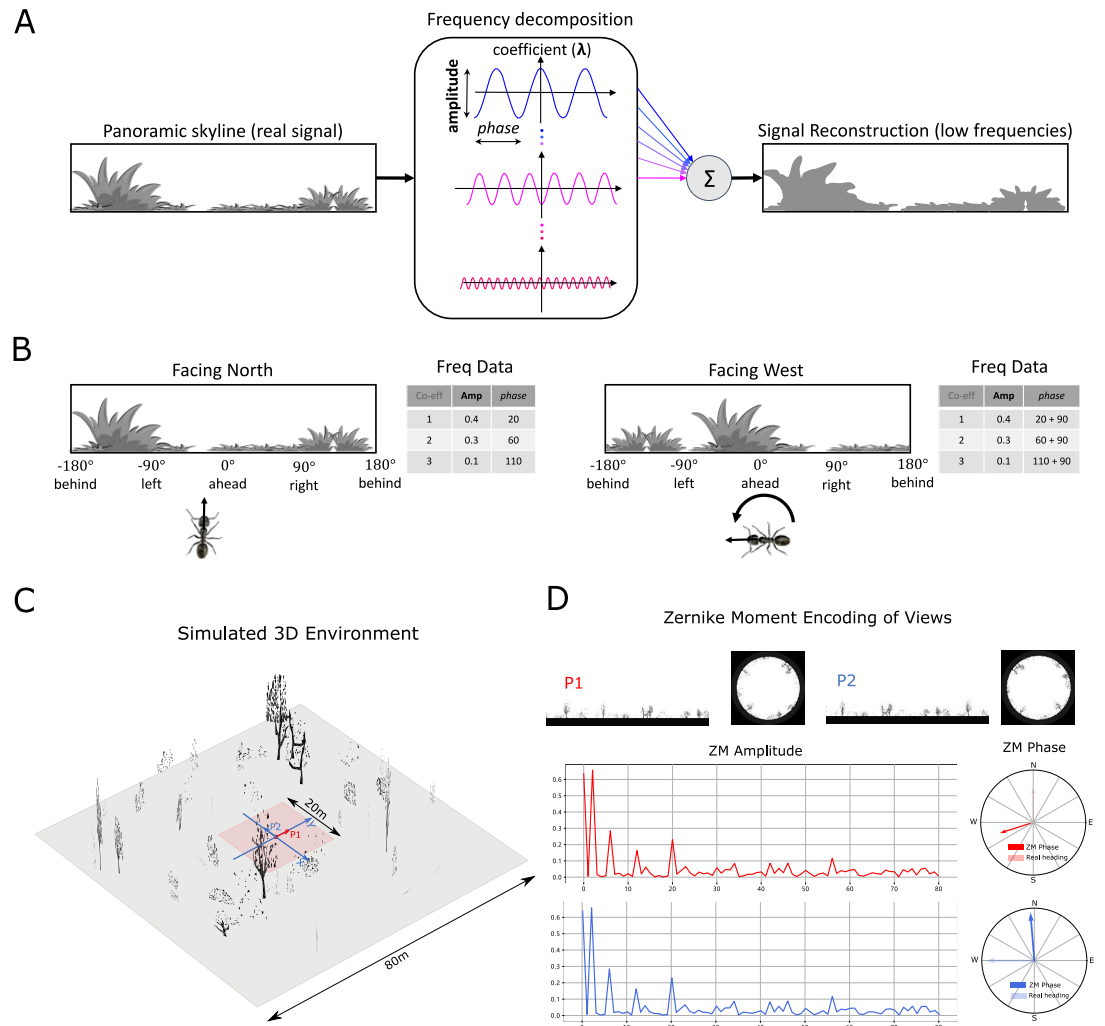


Figure 6. Information provided by frequency encoding in cartoon and simulated ant environments. (A): A cartoon depiction of a panoramic skyline, its decomposition into trigonometric functions, and reconstruction through the summation of low frequency coefficients reflecting standard image compression techniques. **(B):** Following a 90° rotation there is no change in the **amplitudes** of the frequency coefficients but the **phases** of the frequency coefficients track the change in orientation providing a rotational invariant signal useful for visual homing and rotationally-varying signal useful for route following respectively. **(C):** The simulated 3D world used for all experiments. The pink area (size: 20m x 20m) is used for model training and testing zone for models allowing obstacle-free movement. **(D):** The frequency encoding (Zernike Moment’s **amplitudes** and **phase**) of the views sampled from the same location but with different headings (P1 and P2 in **(C)**), with 90° heading difference) in the simulated world. The first 81 **amplitudes** are identical while the **phases** have the difference of about 90°.

Figure 6-source data 1. The matrix of simulated 3D world.

444 **Image processing**

445 Frequency encoding conceptual overview

446 Image compression algorithms such as JPEG encoding (Hudson et al., 2018) have long utilised the
 447 fact that a complex signal can be decomposed into a series of trigonometric functions that oscillate
 448 at different frequencies. The original signal can then be reconstructed by summing all (for perfect
 449 reconstruction) or some (for approximate reconstruction) of the base trigonometric functions.
 450 Thus, compression algorithms seek a balance between using the fewest trigonometric functions to
 451 encode the scene (for example, by omitting high frequencies that humans struggle to perceive), and
 452 the accuracy of the reconstructed signal (often given as an option when converting to JPEG format).

453 **Figure 6A** provides a cartoon of the frequency decomposition process for a panoramic view.

454 When such transforms are applied to fully panoramic images, or skylines, benefits beyond
 455 compression arise. Specifically, discrete transformation algorithms used to extract the frequency
 456 information generate a series of information triplets to describe the original function: frequency
 457 coefficients describe the frequency of the trigonometric function with associated **amplitudes**
 458 and *phase* values defining the vertical height versus the mean and the lateral position of the
 459 waveform respectively (**Figure 6A**). For panoramic views, regardless of the rotational angle of the
 460 image capturing device (eye or camera) the entire signal will always be visible and hence the
 461 **amplitudes** of the frequency coefficients do not alter with rotation (**Figure 6B**). This information
 462 has been used for successful place recognition in a series of robot studies (*Pajdla and Hlaváč, 1999*;
 463 *Menegatti et al., 2004*; *Stone et al., 2016*). Most recently (*Stone et al., 2018*) demonstrated that
 464 the difference between the **amplitudes** of the frequency coefficients recorded at two locations
 465 increases monotonically with distance producing an error surface suitable for visual homing. This
 466 feature of the frequency encoding underlies the visual homing results described in Mushroom
 467 bodies as drivers of rotational invariant visual homing.

468 In addition, as the *phase* of each coefficient describes how to align the signal this will naturally
 469 track any rotation in the panoramic view (**Figure 6B**) providing a means to realign with previous
 470 headings. The *phase* components of panoramic images have been utilised previously to derive
 471 the home direction in a visual homing task (*Stürzl and Mallot, 2006*). This feature of the frequency
 472 encoding underlies the route following results described in Route following in the insect brain.

473 The image processing field has created an array of algorithms for deriving the frequency
 474 content of continuous signals (*Jiang et al., 1996*; *Gonzalez et al., 2004*). To allow exploration of the
 475 usefulness of frequency information, and how it could be used by the known neural structures,
 476 we adopt the same Zernike Moment algorithm used by *Stone et al. (2018)*, but the reader should
 477 be clear that there are many alternate and more biologically plausible processes by which insects
 478 could derive similar information. It is beyond the scope of this proof of concept study to define
 479 precisely how this process might happen in insects but future research possibilities are outlined in
 480 the Discussion.

481 Zernike Moments encoding

482 Zernike Moments (ZM) are defined as the projection of a function onto orthogonal basis polynomials
 483 called Zernike polynomials (*Teague, 1980*; *Khotanzad and Hong, 1990*). This set of functions are
 484 defined on the unit circle with polar coordinates (ρ, θ) shown as:

$$V_{nm}(\rho, \theta) = R_{nm}(\rho)e^{im\theta} \quad (1)$$

485 Where $n \in \mathbb{N}^+$ is the order and m is the repetition meeting the condition: $m \in \mathbb{N}$, $|m| \leq n$ and
 486 $n - |m|$ is even to ensure the rotational invariant property is met. $R_{nm}(\rho)$ is the radial polynomial
 487 defined as:

$$R_{nm}(\rho) = \sum_{s=0}^{n-|m|/2} (-1)^s \frac{(n-s)!}{s!(\frac{n+|m|}{2}-s)!(\frac{n-|m|}{2}-s)!} \rho^{n-2s} \quad (2)$$

488 For a continuous image function $f(x, y)$, the ZM coefficient can be calculated by:

$$Z_{nm}(\rho) = \frac{n+1}{\pi} \int \int_{x^2+y^2 \leq 1} f(x, y) V_{nm}^*(\rho, \theta) dx dy \quad (3)$$

489 For a digital image, summations can replace the integrals to give the ZM:

$$Z_{nm}(\rho) = \frac{n+1}{\pi} \sum_x \sum_y f(x, y) V_{nm}^*(\rho, \theta), \quad x^2 + y^2 \leq 1. \quad (4)$$

490 ZM are extracted from the simulated insect views in wrapped format (**Figure 6D**) whose centre
 491 is taken to be the origin of the polar coordinates such that all valid pixels lie within the unit circle.

492 For a given image I (P1 in **Figure 6D**) and the rotated version of this image I^{θ_r} (P2 in **Figure 6D**), the
 493 **amplitude** $A = |Z|$ and **phase** $\Phi = \angle Z$ of ZM coefficients of these two images will satisfy:

$$\begin{cases} |Z_{nm}^{\theta_r}| = |Z_{nm} e^{-jm\theta_r}| = |Z_{nm}| \quad i.e., \quad A_{nm}^{\theta_r} = A_{nm} \\ \Phi_{nm}^{\theta_r} = \Phi_{nm} - m\theta_r \end{cases} \quad (5)$$

494 From which we can see that the **amplitude** of the ZM coefficient remains the same while the **phase**
 495 of ZM carries the information regarding the rotation (see **Figure 6A** and **D**). This property is the
 496 cornerstone of the visual navigation model where the **amplitudes** encode the features of the view
 497 while the **phase** defines the orientation.

498 **Amplitudes** for ZM orders ranging from $n = 0$ to $n = 16$ were selected as they appeared to cover
 499 the majority of information within the image. From **Equation 1** we know that $V_{n,m} = V_{n,-m}$, so we
 500 limited $m \in N^+$ to reduce the computational cost, which sets the total number of ZM coefficients
 501 (N_{ZM}) to $(16 \div 2 + 1)^2 = 81$ which was input to the visual navigation networks. For training the ANN
 502 network for RF, in **Equation 5**, if we set $m = 1$, such that $\Phi_{n,1}^{\theta_r} = \Phi_{n,1} - \theta_r$ which means that all ZM
 503 coefficients will provide the same information when the image is rotated. Further, the difference
 504 between the **phase** of ZM coefficients of the current view with those of the memorised view, will
 505 inherently provide the angle with which to turn to realign oneself, i.e. :

$$\Phi_{7,1}^{current} - \Phi_{7,1}^{memory} = \theta_n - \theta_m \quad (6)$$

506 Where the order n of this ZM is selected to be $n = 7$ manually by comparing the performance
 507 with different orders in this specific virtual environment, θ_n is the current heading of the agent while
 508 θ_m is the memorised heading direction (desired heading direction).

509 Neural networks

510 We use the simple firing rate to model the neurons in the proposed networks, where the output
 511 firing rate C is a sigmoid function of the input I if there is no special note. In the following
 512 descriptions and formulas, a subscript is used to represent the layers or name of the neuron while
 513 the superscript is used to represent the value at a specific time or with a specific index.

514 Current headings

515 In the proposed model, there are two independent compass systems based on the global and the
 516 local cues respectively so named global and local compass correspondingly. These two compass
 517 systems have similar neural pathways from OL via AOTU and BU to the CX but ended distinct
 518 groupings of TB1 neurons: I-TB1 and II-TB1 in the PB.

519 Global compass

520 The global compass neural network applied in this study is the same as that of **Stone et al. (2017)**,
 521 which has three layers of neurons: TL neurons, CL1 neurons and I-TB1 neurons. The 16 TL neurons
 522 respond to simulated polarised light input and are directly modelled as:

$$I_{TL} = \cos(\theta_{TL} - \theta_h) \quad (7)$$

523 Where $\theta_{TL} \in \{0, \pi/4, \pi/2, 3\pi/4, \pi, 5\pi/4, 3\pi/2, 7\pi/4\}$ is the angular preference of the 16 TL-neurons.
 524 The 16 CL1-neurons are inhibited by TL-neuron activity which invert the polarisation response:

$$I_{CL1} = 1.0 - C_{TL} \quad (8)$$

525 The 8 I-TB1 neurons act as a ring attractor creating a sinusoidal encoding of the current heading.
 526 Each I-TB1 neuron receives excitation from the CL1 neuron sharing the same directional preference
 527 and inhibition from other I-TB1 neurons via mutual connections:

$$W_{I-TB1}^{ij} = \frac{\cos(\theta_{I-TB1}^i - \theta_{I-TB1}^j) - 1}{2} \quad (9)$$

$$I_{I-TB1}^{t,j} = (1 - c)C_{CL1}^{t,j} + c \sum_{i=1}^8 W_{I-TB1}^{ij} C_{I-TB1}^{t-1,j} \quad (10)$$

528 Where c is a balance factor to modify the strength of the inhibition and the CL1 excitation. Finally,
529 the population coding $C_{I-TB1}^{t,j}$, $j = 0, 1, \dots, 7$ represents the heading of global compass of the agent at
530 time t .

531 Local compass

532 The local compass is derived from the terrestrial cues through a similar visual pathway as the global
533 compass and also ends in a ring attractor network. As for the global compass, the local compass
534 heading is directly modelled by the population encoding of II-TB1 neurons:

$$C_{II-TB1}^i = \cos(\Phi_{7,1} - \theta_{II-TB1}^i) \quad i = 0, 1, \dots, 7 \quad (11)$$

535 Where θ_{II-TB1} is the angular preference of the II-TB1 neurons and $\Phi_{7,1}$ is the *phase* of ZM. Therefore,
536 the firing rate of C_{II-TB1} encodes the heading of the local compass.

537 Visual homing

538 The neural network of visual homing is an associative network constrained by the anatomical
539 structure of the mushroom body (MB) of the insects. In contrast to *Ardin et al. (2016)* where a
540 spiking neural network is implemented to model the MB, we apply a simple version of MB where
541 the average firing rates of neurons are used.

542 The visual projection neurons (vPNs) directly receive the **amplitudes** of the ZM coefficients as
543 their firing rates:

$$C_{vPN}^i = A^i, \quad i = 0, 1, 2, \dots, N_{vPN} \quad (12)$$

544 Where N_{vPN} is the number of the vPN neurons which is the same as the total number of ZM
545 **amplitudes** applied and in this study $N_{vPN} = N_{ZM} = 81$. The A^i denotes the i^{th} **amplitudes** of ZM
546 coefficients.

547 The vPNs project into Kenyon cells (KC) through randomly generated binary connections W_{vPN2KC} ,
548 which result in the scenario wherein one KC receives 10 randomly selected vPNs' activation:

$$I_{KC}^j = \sum_{i=0}^{N_{vPN}} W_{vPN2KC}^{ji} C_{vPN}^i \quad (13)$$

549 Where I_{KC}^j denotes the total input current of j^{th} KC from the vPN and the KCs are modelled as
550 binary neurons with the same threshold Thr_{kc} :

$$C_{KC} = \begin{cases} 0 & \text{if } I_{KC} \leq Thr_{KC} \\ 1 & \text{if } I_{KC} > Thr_{KC} \end{cases} \quad (14)$$

551 The MBON neuron sums all the activation of Kenyon cells via plastic connections W_{KC2EN} :

$$C_{MBON} = \sum_{i=0}^{N_{KC}} W_{KC2MBON}^i C_{KC}^i \quad (15)$$

552 An anti-Hebbian learning rule is applied for the plasticity of $W_{KC2MBON}$ in a simple way:

$$W_{KC2MBON}^t = W_{KC2MBON}^{t-1} - \eta_{KC2MBON} \quad \text{if } C_{KC}^i \geq W_{KC2MBON}^i \quad (16)$$

553 Where $\eta_{KC2MBON}$ is the learning rate. The learning process will happen only when the reward signal
554 is turned on. The activation of EN C_{MBON} represents the familiarity of the current view and the
555 change of the C_{MBON} is defined as:

$$\Delta C_{MBON} = C_{MBON}^t - C_{MBON}^{t-1} \quad (17)$$

556 ΔC_{MBON} is used to track the gradient of the familiarity to guide the agent to the more familiar
 557 locations by shifting the I-TB1 neurons' activation C_{I-TB1} .

$$C_{VH}^i = C_{I-TB1}^j, j = \begin{cases} i + offset & \text{if } i + offset \leq 7 \\ i + offset - 7 & \text{otherwise} \end{cases} \quad i = 0, 1, \dots, 7 \quad (18)$$

558 The relationship between the ΔC_{MBON} and the *offset* is shown as following:

$$offset = \begin{cases} 0 & \text{if } \Delta C_{MBON} < 0 \\ \min(\lfloor k_{VH} \Delta C_{MBON} \rfloor, 4) & \text{otherwise} \end{cases} \quad (19)$$

559 Path integration

560 The PI model implemented is that published by *Stone et al. (2017)*. The core functionality arises
 561 from the CPU4 neurons that integrate the activation of TN2 neurons that encode the speed of
 562 the agent and the inverted activation of direction-sensitive I-TB1 neurons. The result is that the
 563 population of CPU4 neurons iteratively track the distance and orientation to the nest (a home
 564 vector) in a format akin to a series of directionally-locked odometers.

565 The firing rate of the CPU4 neurons are updated by:

$$I_{CPU4}^t = I_{CPU4}^{t-1} + r(C_{TN2}^t - C_{I-TB1}^t - k) \quad (20)$$

566 Where the rate of the memory accumulation $r = 0.0025$; the memory loss $k = 0.1$; the initial memory
 567 charge of CPU4 neurons $I_{CPU4}^0 = 0.1$.

568 The input of the TN2 neurons encoding the speed is calculated by:

$$\begin{cases} I_{TN2L} = [\sin(\theta_h + \theta_{TN2}) \cos(\theta_h + \theta_{TN2})] \mathbf{v} \\ I_{TN2R} = [\sin(\theta_h - \theta_{TN2}) \cos(\theta_h - \theta_{TN2})] \mathbf{v} \end{cases} \quad (21)$$

569 where \mathbf{v} is the velocity (see *Equation 39*) of the agent and θ_{TN2} is the preference angle of the TN2
 570 neurons. In this study $\theta_{TN2} = \pi/4$. The activation function applied to TN2 neurons is the rectified
 571 linear function given by:

$$C_{TN2} = \max(0, 2I_{TN2}) \quad (22)$$

572 As CPU4 neurons integrate the speed and direction of the agent, the desired heading of PI can be
 573 represented by the population encoding of these neurons, thus:

$$C_{PI} = C_{CPU4} \quad (23)$$

574 Route Following

575 The route following model is based on a simple artificial neural network (ANN) with just one hidden
 576 layer. The input layer directly takes the **amplitudes** of the ZM coefficients as the activation in the
 577 same way as that of visual projection neurons in MB network. This is a fully connected neural
 578 network with the sigmoid activation function, so the forward propagation is ruled by:

$$\begin{cases} Z_l^i = \sum_{j=0}^N W^{ji} Y_{l-1}^j \\ Y_l^i = \text{sigmoid}(Z_l^i) = \frac{1}{1+e^{-Z_l^i}} \end{cases} \quad i = 0, 1, \dots, 7 \quad \text{and} \quad l = 0, 1, 2 \quad (24)$$

579 Where Z_l^i and Y_l^i denote the input and output of the i^{th} neuron in l^{th} layer, thus the input is the
 580 same as the MB network $Z_0^i = A^i, i = 0, 1, \dots, N_{ZM}$ and the output of the ANN is consequently the
 581 population coding of the RF desired heading, i.e.:

$$C_{RF}^i = Y_i^2 \quad i = 0, 1, \dots, 7 \quad (25)$$

582 For a fast and efficient implementation, the learning method applied here is back propagation
 583 with gradient descend. Training data is derived from the **amplitudes** and the population encoded
 584 *phases* of the ZM coefficients of the images reconstructed along a habitual route. As shown in

585 **Equation 11** the II-TB1 neurons encode the heading of local compass, therefore, the training pair
 586 for the RF network can be defined as $\{A, C_{II-TB1}\}$. After training, this network will correlate the
 587 desired ZM *phase* with the specific ZM **amplitudes**, and when RF is running, the output of this
 588 neural network C_{RF} will represent the desired heading with respect to the current heading of the
 589 local compass represented by the population encoding of II-TB1 neurons.

590 Coordination of elemental guidance strategies

591 The coordination of the three main navigation strategies PI, VH and RF are realised in distinct
 592 stages. Firstly, Off-route strategies (PI and VH) are optimally integrated by weighing according to
 593 the certainty of each before a context-dependent switch activates either On-route (RF) or Off-route
 594 strategies depending on the current visual novelty.

595 Optimal cue integration

596 A ring attractor neural network is used to integrate the cues from the VH and PI guidance systems.
 597 As reported in **Hoinville and Wehner (2018)** summation of directional cues represented in vector
 598 format leads to optimal angular cue integration which is the same case as real insects. **Sun et al.**
 599 **(2018)** gave a biology plausible way to do this kind of computation based on a simple ring attractor
 600 neural network. There are two populations of neurons in this network, the first is the integration
 601 neurons (IN) which is the output population of the network. Constrained by the number of columns
 602 in each hemisphere of the insects CX, we set the number of the IN to be 8, and its firing rate is
 603 updated by:

$$\tau \frac{dC_{IN}}{dt} = -C_{IN} + g \left(\sum_{j=1}^n W_{E2E}^{ji} C_{IN}^j + X_1^i + X_2^i + W_{I2E} C_{UI} \right) \quad i = 0, 1, \dots, 7. \quad (26)$$

604 Where W_{E2E}^{ji} is the recurrent connections from j^{th} neuron to i^{th} neuron, $g(x)$ is the activation function
 605 that provides the non-linear property of the neuron:

$$g(c) = \max(0, \rho + c) \quad (27)$$

606 Where ρ denotes the offset of the function.

607 In **Equation 26**, X_1 and X_2 generally denote the cues that should be integrated. In this study,
 608 X_1 and X_2 represent the desired heading of path integration (C_{PI}) and visual homing (C_{VH}). The
 609 desired heading of PI is also tuned by the tuning neuron (TUN) in SMP which is stimulated by the
 610 MBON of MB (see **Figure 3A**) and its activation function is defined by a rectified linear function, i.e.:

$$C_{TUN} = \min(k_{TUN} C_{EN}, 1) \quad (28)$$

611 Where k_{TUN} is the scaling factor.

612 Thus, the X_1 and X_2 for this ring attractor network can be calculated by:

$$\begin{cases} X_1^i = C_{TUN} C_{PI}^i \\ X_2^i = C_{VH}^i \end{cases} \quad i = 0, 1, \dots, 7 \quad (29)$$

613 The second population of the ring attractor is called the uniform inhibition (UI) neurons modelled
 614 by:

$$\tau \frac{dC_{UI}}{dt} = -u + g \left(W_{I2I} C_{UI} + W_{E2I} \sum_{k=1}^n C_{IN}^k \right) \quad i = 0, 1, \dots, 7. \quad (30)$$

615 After arriving at a stable state, the firing rate of the integration neurons in this ring attractor
 616 network provides the population encoding of the optimal integrated output C_{OI} :

$$C_{OI} = C_{CN} \quad (31)$$

617 Context-dependent switch

618 The model generates two current/desired headings pairs: the current heading of global compass
 619 decoded by C_{I-TB1} with the desired heading optimally integrated by the integration neurons of the
 620 ring attractor network C_{OI} and the current heading of local compass decoded by II-TB1 neurons
 621 C_{II-TB2} with the desired heading decoded by the output of the RF network C_{RF} . These two pairs of
 622 signal both are connected to the steering circuit (see **Figure 5A** and Steering circuit) but are turned
 623 on/off by two switching neurons (SN1 and SN2) in the SMP (**Figure 5A**). SN2 neuron receives the
 624 activation from MBON neuron and is modelled as:

$$SN2 = \begin{cases} 0 & \text{if } C_{MBON} < Thr_{SN2} \\ 1 & \text{otherwise} \end{cases} \quad (32)$$

625 While SN1 will always fire unless SN2 fires:

$$SN1 = \begin{cases} 0 & \text{if } C_{SN2} = 1 \\ 1 & \text{otherwise} \end{cases} \quad (33)$$

626 Therefore, the context-depend switch is achieved according to the current visual novelty represented
 627 by the activation of MBON.

628 Steering circuit

629 The steering neurons, i.e., CPU1 neurons ($C_{CPU1}^i, i = 0, 1, 2, \dots, 15$) receive excitatory input from the de-
 630 sired heading ($C_{DH}^i, i = 0, 1, 2, \dots, 15$) and inhibitory input from the current heading ($C_{CH}, i = 0, 1, 2, \dots, 15$)
 631 to generate the turning signal:

$$C_{ST}^i = C_{DH}^i - C_{CH}^i \quad i = 0, 1, \dots, 15 \quad (34)$$

632 The turning angle is determined by the difference of the activation summations between left
 633 ($i = 0, 1, 2, \dots, 7$) and right ($i = 8, 9, 10, \dots, 15$) set of CPU1 neurons:

$$\theta_M = k_{motor} \left(\sum_{i=0}^7 C_{CPU1}^i - \sum_{i=8}^{15} C_{CPU1}^i \right) \quad (35)$$

634 which corresponds to the difference of the length of the subtracted left and right vectors in
 635 **Figure 2A**. In addition, as it is illustrated in **Figure 2A**, another key part of steering circuit is the
 636 left/right shifted desired heading, in this paper, this is achieved by the offset connectivity pattern
 637 ($W_{DH2CPU1L}$ and $W_{DH2CPU1R}$) from the desired heading to the steering neurons (**Heinze and Homberg,**
 638 **2008; Stone et al., 2017**):

$$\begin{cases} C_{DH}^{0-7} = C_{SN1} C_{RF} W_{DH2CPU1L} + C_{SN2} C_{OI} W_{DH2CPU1L} \\ C_{DH}^{8-15} = C_{SN1} C_{RF} W_{DH2CPU1R} + C_{SN2} C_{OI} W_{DH2CPU1R} \end{cases} \quad (36)$$

639 Where the $W_{DH2CPU1L}$ and $W_{DH2CPU1R}$ are:

$$W_{DH2CPU1L} = \begin{bmatrix} 0 & 1 & 0 & 0 & 0 & 0 & 0 & 0 \\ 0 & 0 & 1 & 0 & 0 & 0 & 0 & 0 \\ 0 & 0 & 0 & 1 & 0 & 0 & 0 & 0 \\ 0 & 0 & 0 & 0 & 1 & 0 & 0 & 0 \\ 0 & 0 & 0 & 0 & 0 & 1 & 0 & 0 \\ 0 & 0 & 0 & 0 & 0 & 0 & 1 & 0 \\ 0 & 0 & 0 & 0 & 0 & 0 & 0 & 1 \\ 1 & 0 & 0 & 0 & 0 & 0 & 0 & 0 \end{bmatrix} \quad W_{DH2CPU1R} = \begin{bmatrix} 0 & 0 & 0 & 0 & 0 & 0 & 0 & 1 \\ 0 & 1 & 0 & 0 & 0 & 0 & 0 & 0 \\ 0 & 0 & 1 & 0 & 0 & 0 & 0 & 0 \\ 0 & 0 & 0 & 1 & 0 & 0 & 0 & 0 \\ 0 & 0 & 0 & 0 & 1 & 0 & 0 & 0 \\ 0 & 0 & 0 & 0 & 0 & 1 & 0 & 0 \\ 0 & 0 & 0 & 0 & 0 & 0 & 1 & 0 \\ 0 & 0 & 0 & 0 & 0 & 0 & 0 & 1 \end{bmatrix} \quad (37)$$

640 which defines the connection pattern realising the left/right shifting of the desired headings
 641 used throughout our model ((**Figure 2A**, **Figure 3A**, **Figure 4A**, **Figure 5A** and **Figure 7A**).

642 The current heading input to the steering circuit is also switched between global and local
 643 compass input via the SN1 and SN2 neuron:

$$\begin{cases} C_{CH}^{0-7} = C_{SN1} C_{II-TB1} + C_{SN2} C_{I-TB1} \\ C_{CH}^{8-15} = C_{SN1} C_{II-TB1} + C_{SN2} C_{I-TB1} \end{cases} \quad (38)$$

644 Detailed neural connectivity of unified model

645 **Figure 7A** shows a complete picture of the proposed model. Specifically, it highlights the final
 646 coordination system showing that CX computing the optimal navigation output with the modulation
 647 from the MB and SMP. In addition, offset connectivity pattern from the desired heading to the
 648 steering circuit that underpin the left/right shifting is clearly shown. **Figure 7BC** shows the network
 649 generating the desired heading of RF and VH respectively.

650 In addition, **Table 1** provides details of all modelled neural circuits with their function and naming
 651 conventions with links to biological evidence for these neural circuits where it exists and the animal
 652 that they were observed in.

653 Simulations

654 **Equation 35** gives the turning angle of the agent, thus the instantaneous "velocity" (v) at every step
 655 can be computed by:

$$v^i = S_L [\cos \theta_M^i, \sin \theta_M^i] \quad (39)$$

656 Where S_L is the step length with the unit of centimetres. Note that we haven't defined the time
 657 accuracy for every step of the simulations, thus the unit of the velocity in this implementation is
 658 $cm/step$ rather than cm/s . Then the position of agent P^{i+1} in the Cartesian coordinates for the is
 659 updated by:

$$P^{i+1} = P^i + v^i \quad (40)$$

660 The main parameter settings for all the simulations in this paper can be found in **Table 2**.

661 Reproduce visual navigation behaviour

662 Inspired by the benchmark study of real ants in **Wystrach et al. (2012)**, we test our model of VH and
 663 RF by reproducing the homing behaviours in that study. This is achieved by constructing a habitual
 664 route with a similar shape (arc or banana shape) in our simulated 3D world. The position P_{R-Arc}
 665 and heading θ_{R-Arc} along that route is manually generated by:

$$\begin{cases} \theta_{R-Arc}^i = \frac{\pi}{2} - i \frac{\pi}{2N_M} \\ P_{R-Arc}^i = [-R \sin \theta_{R-Arc}^i, -7 + R \cos \theta_{R-Arc}^i] \end{cases} \quad i = 0, 1..N_M \quad (41)$$

666 Where the $R = 7m$ is the radius of the arc and $N_M = 20$ in this case is the number of the sampling
 667 points where view images are reconstructed along the route. The reconstructed views then be
 668 wrapped and decomposed by ZM into **amplitudes** and *phases* are used to train the ANN network
 669 of RF and MB network of VH.

670 Visual homing

671 After training, 12 agents with different initial headings that were evenly distributed in $[0, 360)$ were
 672 released at the sideways release point ($P = [0, -7]$) for the simulation of VH (**Figure 2D**). The
 673 headings of the agents at radius 2.5m from the release point (manually selected to ensure that the
 674 all the agents have completed any large initial loop) are taken as the initial headings.

675 Route following

676 After training, 2 agents with 0° and 180° are released at the different release points ($P = [-9, -7]$,
 677 $[-8, -7]$, $[-7, -7]$, $[-6, -7]$, $[-5, -7]$) for the simulation of RF (see **Figure 4B**) to generate the homing
 678 path. And then, we release 12 agents on the route ($P = [-7, -7]$) with different initial headings
 679 that is evenly distributed in $[0, 360)$ to compare the results with the real ant data in **Wystrach et al.**
 680 **(2012)**. The heading of each agent at the position that is 0.6m from the release point is taken as the
 681 initial heading.

Table 1. The details of the main neurons used in the proposed model

Name	Function	Num	Network	Brain region	Neuron in Species(e.g.)	Reference
I-TB1	Global compass current heading	8	Ring attractor		TB1 in <i>Schistocerca gregaria</i> and <i>Megalopta genalis</i>	Heinze and Homberg (2007) Stone et al. (2017)
II-TB1	Local compass current heading	8	Ring attractor		$\Delta 7$ in <i>Drosophila</i>	Franconville et al. (2018)
S I-TB1	Copy of shifted global heading	8	Ring		No data	/
VH-L	VH desired heading left	8	Ring	CX	No data	
VH-R	VH desired heading right	8	Ring		No data	
PI-L	PI desired heading left	8	Ring		CPU4 in <i>Schistocerca gregaria</i> and <i>Megalopta genalis</i>	Heinze and Homberg (2008) Stone et al. (2017)
PI-R	PI desired heading right	8	Ring		P-F3N2v in <i>Drosophila</i>	Franconville et al. (2018)
RF-L	RF desired heading left	8	Ring		No data	
RF-R	RF desired heading right	8	Ring		No data	/
RA-L	Cue integration left	8	Ring attractor		No data	
RA-R	Cue integration right	8	Ring attractor		No data	
CPU1	Comparing the current and desired heading	16	Steering circuit		CPU1 in <i>Schistocerca gregaria</i> and <i>Megalopta genalis</i> PF-LCRe in <i>Drosophila</i>	Heinze and Homberg (2008) Stone et al. (2017) Franconville et al. (2018)
vPN	visual projection	81			MB neurons in <i>Drosophila</i>	Aso et al. (2014)
KCs	Kenyon cells	4000	Associative learning	MB	<i>Camponotus</i>	Ehmer and Gronenberg (2004)
MBON	visual novelty	1			<i>Apis mellifera</i>	Rybak and Menzel (1993)
TUN	Tuning weights from PI to RA	1	/		No data	
SN1	Turn on/off the RF output to CPU1	1	Switch circuit	SMP	No data	/
SN2	Turn on/off the RA output to CPU1	1	Switch circuit		No data	

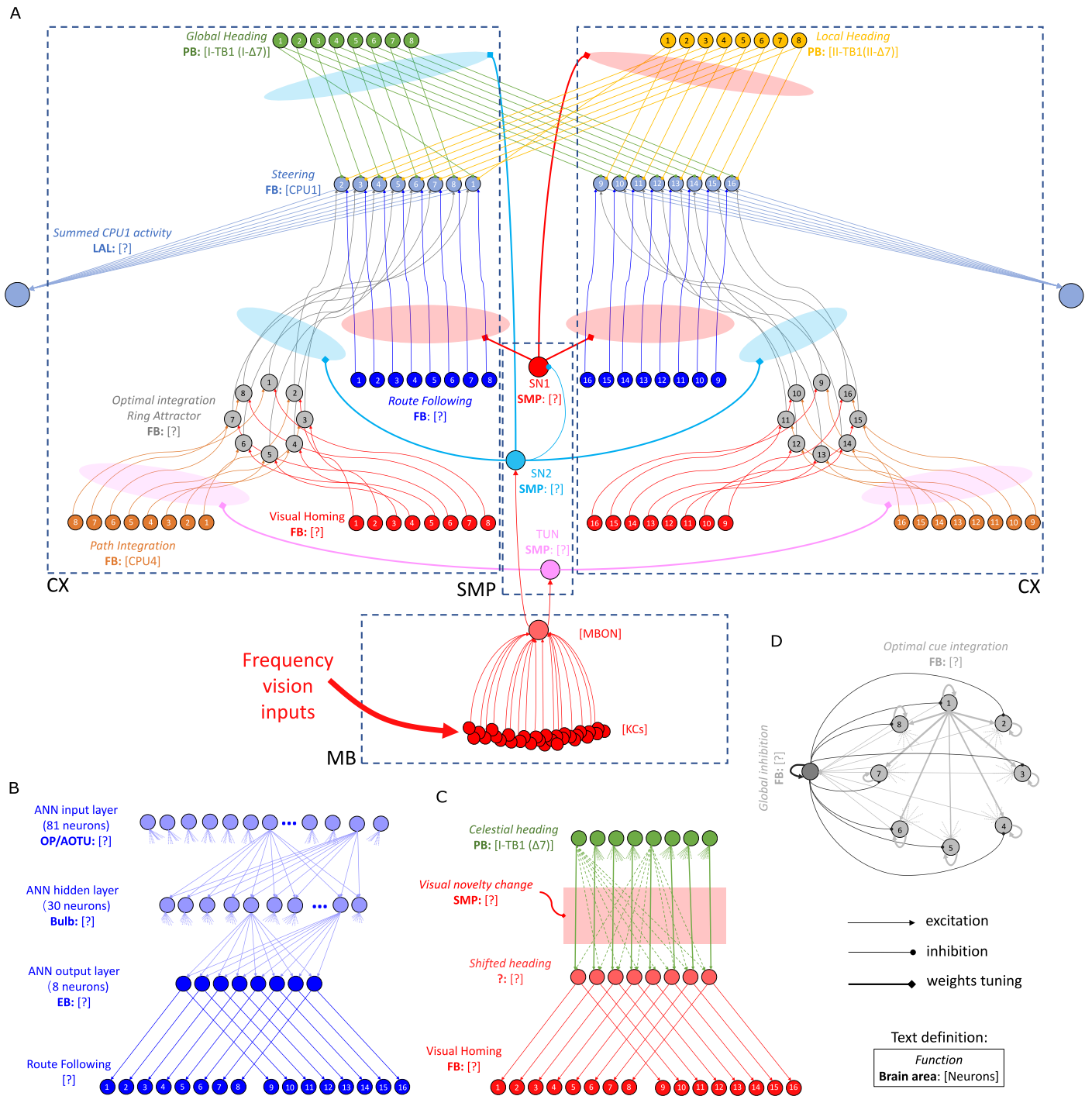


Figure 7. The detailed neural connections of the proposed model. (A): The detailed neural connections of the navigation coordination system. **(B):** The neural connection of the route following network. The input layer to the hidden layer is fully connected, so does the hidden layer to the output layer. **(C):** The network generating the visual homing memory. **(D):** The detailed neural connection of the ring attractor network for optimal cue integration.

682 Reproduce the optimal cue integration behaviour

683 We evaluated the cue integration model by reproducing the results of *Wystrach et al. (2015)* and

684 *Legge et al. (2014)*. The ants' outbound routes in *Wystrach et al. (2015)* is bounded by the corridor,

Table 2. The detailed parameters settings for the simulations

Para.	Visual Homing	Optimal Integration tuning PI	Optimal Integration tuning VH	Route Following	Whole model ZV	Whole model FV
Thr_{KC} (14)	0.04	0.04	0.04	0.04	0.04	0.04
$\eta_{KC2MBON}$ (16)	0.1	0.1	0.1	0.1	0.1	0.1
k_{VH} (19)	2.0	2.0	2.0	/	0.5	0.5
k_{TUN} (28)	/	0.1	0.1	/	0.025	0.0125
Thr_{SN2} (32)	/	/	/	/	2.0	3.0
k_{motor} (35)	0.125	0.125	0.125	0.125	0.375	0.375
S_L (cm/step) (39)	4	4	4	4	8	8
initial heading (deg)	0~360	0~360	0~360	0 / 180	90	0

685 so here we simulate the velocity of the agent by:

$$\mathbf{v}_{out}^t = [rand(0, 2V_0) - V_0, V_0], \quad t = 0, 1 \dots T_{out} \quad (42)$$

686 Where the function $rand(0, x)$ generates a random value from the uniform distribution of $[0, x]$, thus
687 the speed of x-axis will be in $[-V_0, V_0]$ and will cancel each other during the forging. The speed of
688 y-axis is constant so it will accumulated and be recorded by the PI model. And $V_0 = 1cm/step$ is the
689 basic speed of the agent and T_{out} is the total time for outbound phase determining the length of
690 the outbound route. As for the simulated homing route, we duplicate the outbound route when
691 $T_{out} = 300$ but with a inverted heading direction. And then the visual navigation network was trained
692 with images sampled along a simulated route (grey curve in **Figure 3B**).

693 Tuning PI uncertainty

694 The agent in this simulation was allowed to forage to different distances of 0.1m, 1m, 3m or 7m
695 from the nest to accrue different PI states and directional certainties before being translated to a
696 never-before-experienced test site 1.5m from the nest. (RP1 in **Figure 3B**). For each trial, we release
697 20 agents with different initial headings that is evenly distributed in $[0, 360]$. The headings of every
698 agent at the position that is 0.6m from the start point is taken as the initial headings, and the mean
699 direction and the 95% confidential intervals are calculated. As in the biological experiment, the
700 angle between the directions recommended by the PI and visual navigation systems differed by
701 approximately 130° .

702 As the length of the home vector increase (0.1m -> 7m) the activation of PI memory becomes
703 higher (**Figure Supplement 1B**), and increasingly determines the output of the ring attractor inte-
704 gration. Since the length of the home vector is also encoded in the activation of the PI memory
705 neurons, the ring attractor can extract this information as the strength of the cue. As the visual
706 familiarity is nearly the same in the vicinity of the release point, the strength of visual homing circuit
707 remains constant and has more of an influence as the PI length drops.

708 Tuning visual uncertainty

709 The agent in this simulation was allowed to forage up to 1m from the nest to accrue its PI state and
710 directional certainty before being translated to three different release points (RP1, RP2 and RP3 in
711 **Figure 3B**). As the distance from nest increases (RP1->RP2->RP3) so does the visual uncertainty. For
712 each trial, we release 12 agents with different initial headings that is evenly distributed in $[0, 360]$.
713 The headings of each agent at the position that is 0.3m from the start point is taken as the initial
714 headings, and the mean direction and the 95% confidential intervals are calculated.

715 Whole model

716 The simulated habitual route remains the same as in the simulation of visual navigation (Reproduce
717 visual navigation behaviour) as is the learning procedure. The zero- and full- vector agents are both

718 released at $[-2, -7]$ with the heading 0° and 90° respectively. The full-vector agent's PI memory is
 719 generated by letting the agent forage along the route from nest to feeder.

720 Acknowledgements

721 This research has received funding from the European Union's Horizon 2020 research and innovation
 722 programme under the Marie Skłodowska-Curie grant agreement No 778062, ULTRACEPT and No
 723 691154, STEP2DYNA.

724 Thanks to Barbara Webb and Insects Robotics Group at the Univ of Edinburgh, Hadi Maboudi,
 725 Alex Cope and Andrew Philippides for comments on early drafts, and to Antoine Wystrach for
 726 provision of data from previous works. Thanks for proof readers Anne & Mike Mangan (Snr). Finally,
 727 thanks to our editor and reviewers who helped improve the model and manuscript through their
 728 excellent feedback.

729 References

- 730 **Ardin P**, Peng F, Mangan M, Lagogiannis K, Webb B. Using an Insect Mushroom Body Circuit to Encode
 731 Route Memory in Complex Natural Environments. *PLoS Computational Biology*. 2016; doi: [10.1371/jour-](https://doi.org/10.1371/journal.pcbi.1004683)
 732 [nal.pcbi.1004683](https://doi.org/10.1371/journal.pcbi.1004683).
- 733 **Aso Y**, Hattori D, Yu Y, Johnston RM, Iyer NA, Ngo TTB, Dionne H, Abbott LF, Axel R, Tanimoto H, Rubin GM. The
 734 neuronal architecture of the mushroom body provides a logic for associative learning. *eLife*. 2014; 3:e04577.
 735 doi: [10.7554/eLife.04577](https://doi.org/10.7554/eLife.04577).
- 736 **Baddeley B**, Graham P, Husbands P, Philippides A. A model of ant route navigation driven by scene familiarity.
 737 *PLoS Computational Biology*. 2012; doi: [10.1371/journal.pcbi.1002336](https://doi.org/10.1371/journal.pcbi.1002336).
- 738 **Barth M**, Heisenberg M. Vision affects mushroom bodies and central complex in *Drosophila melanogaster*.
 739 *Learning & Memory*. 1997; 4(2):219–229.
- 740 **Betz MJ**, el Jundi B, Heinze S, Homberg U. Topographic organization and possible function of the posterior
 741 optic tubercles in the brain of the desert locust *Schistocerca gregaria*. *Journal of Comparative Neurology*.
 742 2015; 523(11):1589–1607.
- 743 **Bregy P**, Sommer S, Wehner R. Nest-mark orientation versus vector navigation in desert ants. *Journal of*
 744 *Experimental Biology*. 2008; 211(12):1868–1873.
- 745 **Cartwright B**, Collett T. How honey bees use landmarks to guide their return to a food source. *Nature*. 1982;
 746 295(5850):560.
- 747 **Collett M**. How navigational guidance systems are combined in a desert ant. *Current Biology*. 2012; 22(10):927–
 748 932.
- 749 **Collett M**, Chittka L, Collett TS. Spatial memory in insect navigation. *Current Biology*. 2013; 23(17):R789–R800.
 750 <http://dx.doi.org/10.1016/j.cub.2013.07.020>, doi: [10.1016/j.cub.2013.07.020](https://doi.org/10.1016/j.cub.2013.07.020).
- 751 **Collett M**, Collett TS. How does the insect central complex use mushroom body output for steering? *Current*
 752 *Biology*. 2018; 28(13):R733–R734. <http://dx.doi.org/10.1016/j.cub.2018.05.060>, doi: [10.1016/j.cub.2018.05.060](https://doi.org/10.1016/j.cub.2018.05.060).
- 753 **Collett TS**. Path integration: how details of the honeybee waggle dance and the foraging strategies of desert
 754 ants might help in understanding its mechanisms. *Journal of Experimental Biology*. 2019; 222(11):jeb205187.
- 755 **Collett T**. Insect navigation en route to the goal: multiple strategies for the use of landmarks. *Journal of*
 756 *Experimental Biology*. 1996; 199(1):227–235.
- 757 **Cope AJ**, Sabo C, Vasilaki E, Barron AB, Marshall JAR. A computational model of the integration of landmarks
 758 and motion in the insect central complex. *PLoS ONE*. 2017; 12(2):1–19. doi: [10.1371/journal.pone.0172325](https://doi.org/10.1371/journal.pone.0172325).
- 759 **Cruse H**, Wehner R. No need for a cognitive map: decentralized memory for insect navigation. *PLoS computa-*
 760 *tional biology*. 2011; 7(3):e1002009.
- 761 **Dacke M**, Bell AT, Foster JJ, Baird EJ, Strube-Bloss MF, Byrne MJ, el Jundi B. Multimodal cue integration in the
 762 dung beetle compass. *Proceedings of the National Academy of Sciences*. 2019; p. 201904308.

- 763 **Dewar ADM**, Philippides A, Graham P. What is the relationship between visual environment and the form of
764 ant learning-walks? An in silico investigation of insect navigation. *Adaptive Behavior*. 2014; 22(3):163–179.
765 <https://doi.org/10.1177/1059712313516132>, doi: 10.1177/1059712313516132.
- 766 **Ehmer B**, Gronenberg W. Segregation of visual input to the mushroom bodies in the honeybee (*Apis mellifera*).
767 *Journal of Comparative Neurology*. 2002; 451(4):362–373.
- 768 **Ehmer B**, Gronenberg W. Mushroom body volumes and visual interneurons in ants: comparison between sexes
769 and castes. *Journal of Comparative Neurology*. 2004; 469(2):198–213.
- 770 **El Jundi B**, Foster JJ, Khaldy L, Byrne MJ, Dacke M, Baird E. A snapshot-based mechanism for celestial orientation.
771 *Current biology*. 2016; 26(11):1456–1462.
- 772 **Fisher YE**, Lu J, D'Alessandro I, Wilson RI. Sensorimotor experience remaps visual input to a heading-direction
773 network. *Nature*. 2019; 576(7785):121–125.
- 774 **Fleischmann PN**, Christian M, Müller VL, Rössler W, Wehner R. Ontogeny of learning walks and the acquisition of
775 landmark information in desert ants, *Cataglyphis fortis*. *Journal of Experimental Biology*. 2016; 219(19):3137–
776 3145.
- 777 **Franconville R**, Beron C, Jayaraman V. Building a functional connectome of the *Drosophila* central complex.
778 *eLife*. 2018; 7. doi: [10.7554/elife.37017](https://doi.org/10.7554/elife.37017).
- 779 **Fukushi T**, Wehner R. Navigation in wood ants *Formica japonica*: context dependent use of landmarks. *Journal*
780 *of Experimental Biology*. 2004; 207(19):3431–3439.
- 781 **Gkanias E**, Risse B, Mangan M, Webb B. From skylight input to behavioural output: a computational model of
782 the insect polarised light compass. *PLoS computational biology*. 2019; 15(7):e1007123.
- 783 **Gonzalez RC**, Woods RE, Eddins SL. *Digital image processing using MATLAB*. Pearson Education India; 2004.
- 784 **Graham P**, Philippides A, Baddeley B. Animal cognition: multi-modal interactions in ant learning. *Current*
785 *Biology*. 2010; 20(15):R639–R640.
- 786 **Green J**, Adachi A, Shah KK, Hirokawa JD, Magani PS, Maimon G. A neural circuit architecture for angular
787 integration in *Drosophila*. *Nature*. 2017; 546(7656):101.
- 788 **Gronenberg W**, López-Riquelme G. Multisensory convergence in the mushroom bodies of ants and bees. *Acta*
789 *Biologica Hungarica*. 2004; 55(1-4):31–37.
- 790 **Hanesch U**, Fischbach KF, Heisenberg M. Neuronal architecture of the central complex in *Drosophila*
791 *melanogaster*. *Cell and Tissue Research*. 1989; 257(2):343–366. doi: 10.1007/BF00261838.
- 792 **Harrison JF**, Fewell JH, Stiller TM, Breed MD. Effects of experience on use of orientation cues in the giant tropical
793 ant. *Animal behaviour*. 1989; .
- 794 **Heinze S**. Unraveling the neural basis of insect navigation. *Current Opinion in Insect Science*. 2017; 24(Figure
795 1):58–67. <http://dx.doi.org/10.1016/j.cois.2017.09.001>, doi: [10.1016/j.cois.2017.09.001](https://doi.org/10.1016/j.cois.2017.09.001).
- 796 **Heinze S**, Homberg U. Maplike representation of celestial E-vector orientations in the brain of an insect. *Science*.
797 2007; 315(5814):995–997.
- 798 **Heinze S**, Homberg U. Neuroarchitecture of the central complex of the desert locust: Intrinsic and columnar
799 neurons. *Journal of Comparative Neurology*. 2008; 511(4):454–478. doi: [10.1002/cne.21842](https://doi.org/10.1002/cne.21842).
- 800 **Heinze S**, Homberg U. Linking the input to the output: new sets of neurons complement the polarization vision
801 network in the locust central complex. *Journal of Neuroscience*. 2009; 29(15):4911–4921.
- 802 **Heinze S**, Narendra A, Cheung A. Principles of Insect Path Integration. *Current Biology*. 2018; 28(17):R1043–
803 R1058. <https://doi.org/10.1016/j.cub.2018.04.058>, doi: [10.1016/j.cub.2018.04.058](https://doi.org/10.1016/j.cub.2018.04.058).
- 804 **Heinze S**, Pfeiffer K. The insect central complex—from sensory coding to directing movement. *Frontiers in*
805 *behavioral neuroscience*. 2018; 12:156.
- 806 **Heisenberg M**. Mushroom body memoir: from maps to models. *Nature Reviews Neuroscience*. 2003; 4(4):266.

- 807 **Hoinville T**, Wehner R. Optimal multiguide integration in insect navigation. *Proceedings of the National*
808 *Academy of Sciences*. 2018; 115(11):201721668. <http://www.pnas.org/lookup/doi/10.1073/pnas.1721668115>,
809 [doi: 10.1073/pnas.1721668115](https://doi.org/10.1073/pnas.1721668115).
- 810 **Hoinville T**, Wehner R, Cruse H. Learning and retrieval of memory elements in a navigation task. In: *Conference*
811 *on Biomimetic and Biohybrid Systems* Springer; 2012. p. 120–131.
- 812 **Homborg U**, Hofer S, Pfeiffer K, Gebhardt S. Organization and neural connections of the anterior optic tubercle
813 in the brain of the locust, *Schistocerca gregaria*. *Journal of Comparative Neurology*. 2003; 462(4):415–430.
- 814 **Honkanen A**, Adden A, da Silva Freitas J, Heinze S. The insect central complex and the neural basis of navigational
815 strategies. *The Journal of Experimental Biology*. 2019; 222(Suppl 1):jeb188854. [doi: 10.1242/jeb.188854](https://doi.org/10.1242/jeb.188854).
- 816 **Horridge GA**. Pattern discrimination by the honeybee: disruption as a cue. *Journal of Comparative Physiology*
817 *A*. 1997; 181(3):267–277.
- 818 **Hudson G**, Léger A, Niss B, Sebestyén I, Vaaben J. JPEG-1 standard 25 years: past, present, and future reasons
819 for a success. *Journal of Electronic Imaging*. 2018; 27(4):040901.
- 820 **James A**, Osorio D. Characterisation of columnar neurons and visual signal processing in the medulla of the
821 locust optic lobe by system identification techniques. *Journal of Comparative Physiology A*. 1996; 178(2):183–
822 199.
- 823 **Jeffery KJ**, Page HJ, Stringer SM. Optimal cue combination and landmark-stability learning in the head direction
824 system. *The Journal of physiology*. 2016; 594(22):6527–6534.
- 825 **Jiang H**, Paulsen KD, Osterberg UL, Pogue BW, Patterson MS. Optical image reconstruction using frequency-
826 domain data: simulations and experiments. *JOSA A*. 1996; 13(2):253–266.
- 827 **Kakaria KS**, de Bivort BL. Ring attractor dynamics emerge from a spiking model of the entire protocerebral
828 bridge. *Frontiers in behavioral neuroscience*. 2017; 11:8.
- 829 **Khotanzad A**, Hong YH. Invariant image recognition by Zernike moments. *IEEE Transactions on pattern analysis*
830 *and machine intelligence*. 1990; 12(5):489–497.
- 831 **Kim IS**, Dickinson MH. Idiothetic path integration in the fruit fly *Drosophila melanogaster*. *Current Biology*.
832 2017; 27(15):2227–2238.
- 833 **Kim SS**, Hermundstad AM, Romani S, Abbott L, Jayaraman V. Generation of stable heading representations in
834 diverse visual scenes. *Nature*. 2019; 576(7785):126–131.
- 835 **Kim SS**, Rouault H, Druckmann S, Jayaraman V. Ring attractor dynamics in the *Drosophila* central brain. *Science*.
836 2017; 356(6340):849–853.
- 837 **Kodzhabashev A**, Mangan M. Route following without scanning. In: *Conference on Biomimetic and Biohybrid*
838 *Systems* Springer; 2015. p. 199–210.
- 839 **Kohler M**, Wehner R. Idiosyncratic route-based memories in desert ants, *Melophorus bagoti*: how do they
840 interact with path-integration vectors? *Neurobiology of learning and memory*. 2005; 83(1):1–12.
- 841 **Legge ELG**, Wystrach A, Spetch ML, Cheng K. Combining sky and earth: desert ants (*Melophorus bagoti*) show
842 weighted integration of celestial and terrestrial cues. *Journal of Experimental Biology*. 2014; 217(23):4159–
843 4166. <http://jeb.biologists.org/cgi/doi/10.1242/jeb.107862>, [doi: 10.1242/jeb.107862](https://doi.org/10.1242/jeb.107862).
- 844 **Lehrer M**. Shape perception in the honeybee: symmetry as a global framework. *International Journal of Plant*
845 *Sciences*. 1999; 160(S6):S51–S65.
- 846 **Mangan M**, Webb B. Spontaneous formation of multiple routes in individual desert ants (*Cataglyphis velox*).
847 *Behavioral Ecology*. 2012; 23(5):944–954. [doi: 10.1093/beheco/ars051](https://doi.org/10.1093/beheco/ars051).
- 848 **Menegatti E**, Maeda T, Ishiguro H. Image-based memory for robot navigation using properties of omnidirec-
849 tional images. *Robotics and Autonomous Systems*. 2004; 47(4):251–267.
- 850 **Müller J**, Nawrot M, Menzel R, Landgraf T. A neural network model for familiarity and context learning during
851 honeybee foraging flights. *Biological cybernetics*. 2018; 112(1-2):113–126.
- 852 **Müller M**, Wehner R. Path integration provides a scaffold for landmark learning in desert ants. *Current Biology*.
853 2010; 20(15):1368–1371.

- 854 **Narendra A.** Homing strategies of the Australian desert ant *Melophorus bagoti* II. Interaction of the path
855 integrator with visual cue information. *Journal of Experimental Biology*. 2007; 210(10):1804–1812.
- 856 **O'Carroll D.** Feature-detecting neurons in dragonflies. *Nature*. 1993; 362(6420):541.
- 857 **Ofstad TA, Zuker CS, Reiser MB.** Visual place learning in *Drosophila melanogaster*. *Nature*. 2011; 474. doi:
858 10.1038/nature10131.
- 859 **Omoto JJ, Keleş MF, Nguyen BCM, Bolanos C, Lovick JK, Frye MA, Hartenstein V.** Visual input to the *Drosophila*
860 central complex by developmentally and functionally distinct neuronal populations. *Current Biology*. 2017;
861 27(8):1098–1110.
- 862 **Pajdla T, Hlaváč V.** Zero phase representation of panoramic images for image based localization. In: *International*
863 *Conference on Computer Analysis of Images and Patterns* Springer; 1999. p. 550–557.
- 864 **Paulk AC, Kirszenblat L, Zhou Y, van Swinderen B.** Closed-loop behavioral control increases coherence in the fly
865 brain. *Journal of Neuroscience*. 2015; 35(28):10304–10315.
- 866 **Pfeiffer K, Homberg U.** Organization and functional roles of the central complex in the insect brain. *Annual*
867 *review of entomology*. 2014; 59:165–184.
- 868 **Pisokas I, Heinze S, Webb B.** The heading direction circuit of two insect species. *bioRxiv*. 2019; p. 854521.
- 869 **Plath JA, Entler BV, Kirkerud NH, Schlegel U, Galizia CG, Barron AB.** Different Roles for Honey Bee Mushroom
870 Bodies and Central Complex in Visual Learning of Colored Lights in an Aversive Conditioning Assay. *Frontiers*
871 *in Behavioral Neuroscience*. 2017; 11(May). doi: 10.3389/fnbeh.2017.00098.
- 872 **Reppert SM, Guerra PA, Merlin C.** Neurobiology of monarch butterfly migration. *Annual review of entomology*.
873 2016; 61.
- 874 **Rybak J, Menzel R.** Anatomy of the mushroom bodies in the honey bee brain: the neuronal connections of the
875 alpha-lobe. *Journal of Comparative Neurology*. 1993; 334(3):444–465.
- 876 **Schwarz S, Mangan M, Zeil J, Webb B, Wystrach A.** How ants use vision when homing backward. *Current Biology*.
877 2017; 27(3):401–407.
- 878 **Seelig JD, Jayaraman V.** Feature detection and orientation tuning in the *Drosophila* central complex. *Nature*.
879 2013; 503(7475):262–266. <http://dx.doi.org/10.1038/nature12601>, doi: 10.1038/nature12601.
- 880 **Seelig JD, Jayaraman V.** Neural dynamics for landmark orientation and angular path integration. *Nature*. 2015;
881 521(7551):186–191. doi: 10.1038/nature14446.
- 882 **Steinbeck F, Adden A, Graham P.** Connecting brain to behaviour: a role for general purpose steering circuits in
883 insect orientation? *Journal of Experimental Biology*. 2020; 223(5).
- 884 **Stone T, Differt D, Milford M, Webb B.** Skyline-based localisation for aggressively manoeuvring robots using UV
885 sensors and spherical harmonics. In: *2016 IEEE International Conference on Robotics and Automation (ICRA)*
886 *IEEE*; 2016. p. 5615–5622.
- 887 **Stone T, Mangan M, Wystrach A, Webb B.** Rotation invariant visual processing for spatial memory in insects.
888 *Interface Focus*. 2018; doi: 10.1098/rsfs.2018.0010.
- 889 **Stone T, Webb B, Adden A, Weddig NB, Honkanen A, Templin R, Wcislo W, Scimeca L, Warrant E, Heinze S.** An
890 Anatomically Constrained Model for Path Integration in the Bee Brain. *Current Biology*. 2017; 27(20):3069–
891 3085.e11. <https://doi.org/10.1016/j.cub.2017.08.052>, doi: 10.1016/j.cub.2017.08.052.
- 892 **Stürzl W, Mallot HA.** Efficient visual homing based on Fourier transformed panoramic images. *Robotics and*
893 *Autonomous Systems*. 2006; 54(4):300–313.
- 894 **Stürzl W, Zeil J, Boeddeker N, Hemmi JM.** How wasps acquire and use views for homing. *Current Biology*. 2016;
895 26(4):470–482.
- 896 **Sun X, Mangan M, Yue S.** An analysis of a ring attractor model for cue integration. In: *Conference on Biomimetic*
897 *and Biohybrid Systems* Springer; 2018. p. 459–470.
- 898 **Teague MR.** Image analysis via the general theory of moments. *JOSA*. 1980; 70(8):920–930.

- 899 **Timaeus L**, Geid L, Sancer G, Wernet MF, Hummel T. Parallel visual pathways with topographic versus non-
900 topographic organization connect the *Drosophila* eyes to the central brain. *bioRxiv*. 2020; .
- 901 **Touretzky DS**. Attractor network models of head direction cells. *Head direction cells and the neural mechanisms*
902 *of spatial orientation*. 2005; p. 411–432.
- 903 **Turner-Evans D**, Wegener S, Rouault H, Franconville R, Wolff T, Seelig JD, Druckmann S, Jayaraman V. Angular
904 velocity integration in a fly heading circuit. *Elife*. 2017; 6:e23496.
- 905 **Turner-Evans DB**, Jensen K, Ali S, Paterson T, Sheridan A, Ray RP, Lauritzen S, Bock D, Jayaraman V. The
906 neuroanatomical ultrastructure and function of a biological ring attractor. *bioRxiv*. 2019; p. 847152.
- 907 **Webb B**. The internal maps of insects. *The Journal of Experimental Biology*. 2019; 222(Suppl 1):jeb188094. doi:
908 [10.1242/jeb.188094](https://doi.org/10.1242/jeb.188094).
- 909 **Wehner R**. The architecture of the desert ant's navigational toolkit. *Myrmecological News*. 2009;
910 12(September):85–96.
- 911 **Wystrach A**, Beugnon G, Cheng K. Ants might use different view-matching strategies on and off the route.
912 *Journal of Experimental Biology*. 2012; 215(1):44–55. <http://jeb.biologists.org/cgi/doi/10.1242/jeb.059584>, doi:
913 [10.1242/jeb.059584](https://doi.org/10.1242/jeb.059584).
- 914 **Wystrach A**, Mangan M, Philippides A, Graham P. Snapshots in ants? New interpretations of paradigmatic
915 experiments. *Journal of Experimental Biology*. 2013; 216(10):1766–1770. doi: [10.1242/jeb.082941](https://doi.org/10.1242/jeb.082941).
- 916 **Wystrach A**, Beugnon G, Cheng K. Landmarks or panoramas: what do navigating ants attend to for guidance?
917 *Frontiers in Zoology*. 2011; 8(1):21.
- 918 **Wystrach A**, Lagogiannis K, Webb B. Continuous lateral oscillations as a core mechanism for taxis in *drosophila*
919 larvae. *eLife*. 2016; 5(OCTOBER2016). doi: [10.7554/eLife.15504](https://doi.org/10.7554/eLife.15504).
- 920 **Wystrach A**, Mangan M, Webb B. Optimal cue integration in ants. *Proceedings of the Royal Society B: Biological*
921 *Sciences*. 2015; 282(1816). doi: [10.1098/rspb.2015.1484](https://doi.org/10.1098/rspb.2015.1484).
- 922 **Xu CS**, Januszewski M, Lu Z, Takemura Sy, Hayworth K, Huang G, Shinomiya K, Maitin-Shepard J, Ackerman D,
923 Berg S, et al. A connectome of the adult *drosophila* central brain. *BioRxiv*. 2020; .
- 924 **Yilmaz A**, Grübel K, Spaethe J, Rössler W. Distributed plasticity in ant visual pathways following colour learning.
925 *Proceedings of the Royal Society B*. 2019; 286(1896):20182813.
- 926 **Zeil J**. Visual homing: an insect perspective. *Current opinion in neurobiology*. 2012; 22(2):285–293.
- 927 **Zeil J**, Fleischmann PN. The learning walks of ants (Hymenoptera: Formicidae). *Myrmecological News*. 2019; 29.
- 928 **Zeil J**, Hofmann MI, Chahl JS. Catchment areas of panoramic snapshots in outdoor scenes. *JOSA A*. 2003;
929 20(3):450–469.
- 930 **Zeil J**, Kelber A, Voss R. Structure and function of learning flights in ground-nesting bees and wasps. *Journal of*
931 *Experimental Biology*. 1996; 199(1):245–252.

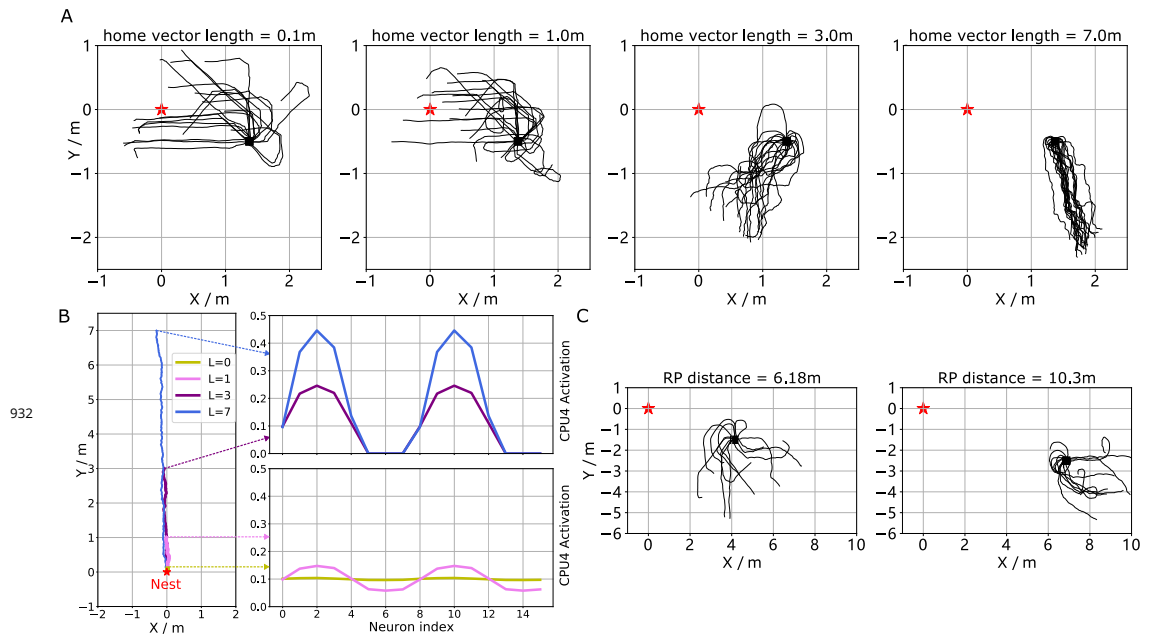


Figure 3-Figure supplement 1. The extended homing paths and the PI memory in the simulations. (A) The extended homing path of 20 agents released at RP1 in **Figure 3B** with different home vector length. **(B)** The activation of CPU4 neurons (PI memory) encoding home vectors with different lengths from 0 to 7.0m. **(C)** The extended homing paths of 20 agents released at RP2 and RP3 in **Figure 3B**.